A constitutive model for plastically anisotropic solids with non-spherical voids

S. M. Keralavarma and A. A. Benzerga

Department of Aerospace Engineering, Texas A&M University

College Station, TX 77843-3141, USA

Abstract

Plastic constitutive relations are derived for a class of anisotropic porous materials consisting of coaxial spheroidal voids, arbitrarily oriented relative to the embedding orthotropic matrix. The derivations are based on nonlinear homogenization, limit analysis and micromechanics. A variational principle is formulated for the yield criterion of the effective medium and specialized to a spheroidal representative volume element containing a confocal spheroidal void and subjected to uniform boundary deformation. To obtain closed form equations for the effective yield locus, approximations are introduced in the limit-analysis based on a restricted set of admissible microscopic velocity fields. Evolution laws are also derived for the microstructure, defined in terms of void volume fraction, aspect ratio and orientation, using material incompressibility and Eshelby-like concentration tensors. The new yield criterion is an extension of the well known isotropic Gurson model. It also extends previous analyses of uncoupled effects of void shape and material anisotropy on the effective plastic behavior of solids containing voids. Preliminary comparisons with finite element calculations of voided cells show that the model captures non-trivial effects of anisotropy heretofore not picked up by void growth models.

Keywords: A. Ductile fracture; A. Voids and inclusions; B. Constitutive behavior; B. Elastic-plastic porous material; C. Upper bound Theory; C. Finite Element Analysis

1 Introduction

Failure in metallic structures at temperatures above the brittle-to-ductile transition typically occurs by the nucleation, growth and coalescence of microvoids (e.g., Pineau and Pardoen, 2007). Understanding the material-specific processes of ductile fracture is central to structural integrity assessment and to failure mitigation in various contexts, from metal forming to high strain-rate penetration phenomena. A generally accepted model of ductile fracture was developed in the 1980's by Tvergaard and Needleman (1984) based on earlier developments in the micromechanics of void growth by McClintock (1968), Rice and Tracey (1969) and most notably Gurson (1977); see (Tvergaard, 1990) for a review. However, many structural materials exhibit pronounced anisotropic deformation, damage and fracture behavior, which cannot be captured using the above isotropic model (Fig. 1). Part of this anisotropy is initial in that it is related to processing and fabrication

routes. The other part is induced: the basic microstructural unit evolves under the large plastic deformations that precede fracture. The key microstructural features involved in anisotropic ductile damage include material texture, grain elongation, deformability of second-phase particles during processing and directionality in the spatial distribution of the latter. While damage initiation mainly occurs at second-phase particles, subsequent accumulation of damage (void growth) is affected by plastic deformation in the matrix.

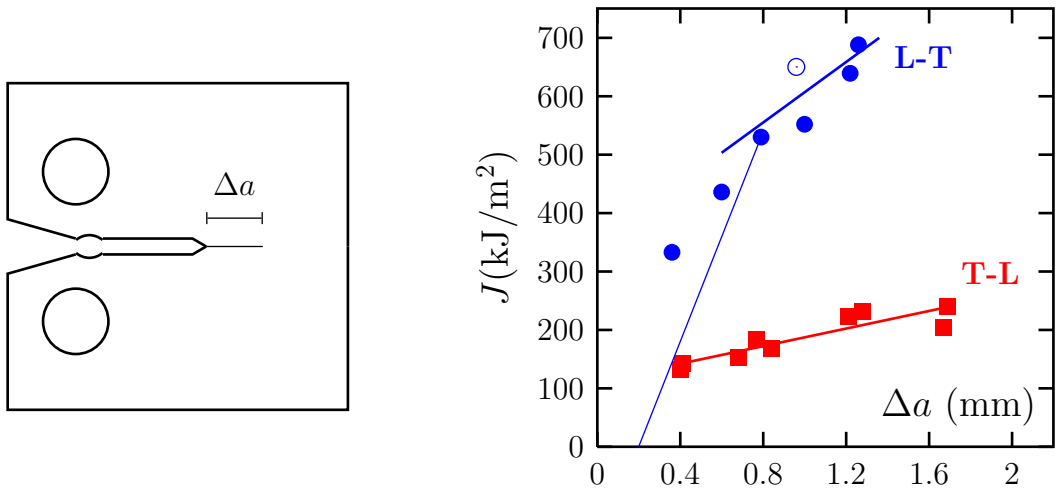

Figure 1: Crack growth resistance curves of a tough pressure vessel C–Mn steel determined using compact-tension specimen testing for two loading orientations: L–T (load along axial direction L with crack extension, Δa, along transverse direction T) and T–L (vice-versa). Values of toughness, J_{Ic}, according to ASTM E-813-94 are 503kJ/m^2 and 121kJ/m^2, respectively. Adapted from (Benzerga, 2000).

Gurson (1977) treated the nonlinear homogenization problem of a representative volume element (RVE) of a porous material subject to axisymmetric loading. His RVE consisted of a hollow *sphere* made up of a rigid, perfectly plastic and *isotropic* material containing a concentric *spherical* void. The outcome of his analysis was an effective yield criterion for the porous material along with an evolution law for the void volume fraction. His derivation was later shown to be amenable to Hill–Mandel homogenization of the kinematic kind, combined with limit-analysis of the chosen RVE subject to *arbitrary* loading conditions; (see e.g. Perrin, 1992; Leblond, 2003). A unique feature of Gurson's criterion is that it constitutes, for the chosen RVE, a rigorous upper bound, which also happens to lie very close to the exact criterion (Leblond, 2003). To account for initial and induced anisotropies, extensions of the Gurson model were developed in the 1990's to incorporate void shape effects (Gologanu et al., 1993, 1994, 1997; Garajeu et al., 2000) and plastic anisotropy of the matrix material (Benzerga and Besson, 2001). Both have been shown to affect void growth to first order. Incorporating void shape effects based on an alternative variational principle using the concept of a linear comparison material (Ponte Castaneda, 1991) are also worthy of note (Ponte Castañeda and Zaidman, 1994; Kailasam and Ponte Castaneda, 1998). It seems reasonable to expect that plastic anisotropy and void shape effects will manifest themselves in the orientation dependence of toughness in some structural materials, as illustrated in Fig. 1.

Micromechanical unit-cell calculations of the type pioneered by Koplik and Needleman (1988) have also documented the effect of void shape on void coalescence (Sovik and

Thaulow, 1997; Pardoen and Hutchinson, 2000). This has motivated the development of improved models of void coalescence (Gologanu, 1997; Gologanu et al., 2001; Benzerga et al., 1999; Benzerga, 2000; Pardoen and Hutchinson, 2000; Benzerga, 2002; Leblond and Mottet, 2008; Scheyvaerts et al., 2010). For further practical implications of using anisotropic models in ductile fracture predictions, see the recent reviews by Pineau (2006) and Pineau and Pardoen (2007).

Based on the above extensions of the Gurson model, Benzerga et al. (2002, 2004) introduced a ductile fracture computational methodology, which accounts for all types of initial and induced anisotropy listed above. In particular, they proposed a heuristic combination of void shape and plastic anisotropy effects. Details may be found in (Benzerga, 2000). More recently, Monchiet et al. (2008) and Keralavarma and Benzerga (2008) have tackled a Gurson–like homogenization problem to obtain a new yield function that truly couples plastic anisotropy and void shape effects. In both investigations, the RVE consisted of a hollow *spheroid* made up of a rigid, perfectly plastic and *orthotropic* material containing a confocal *spheroidal* void. The chief concern of both articles was the derivation of a new effective yield function, not the evolution of microstructure. While Monchiet et al. (2008) derived an approximate yield criterion using a limited description of the microscopic deformation fields, Keralavarma and Benzerga (2008) obtained more accurate results by considering a richer description of those fields. However, in the latter work, the void axis was taken to be aligned with one direction of orthotropy of the matrix material and the loading was axially symmetric about the void axis. In this paper, we develop a more general approximate solution applicable to (i) *non-axisymmetric* loadings; and (ii) under circumstances where the void axis is no longer constrained to be aligned with a principal axis of matrix orthotropy. The latter situation arises, for example, under off-axes loading of hot-rolled steels as a consequence of induced anisotropy, Fig. 2. In addition, we derive micromechanics-based evolution laws for the microstructure. We emphasize that while the remote loading is non-axisymmetric the void is approximated by a spheroid throughout the deformation. This approximation is of no consequence on the potential upper-bound character of the effective yield locus; it may be likened to approximating a void by a sphere in the Gurson model when deviatoric loadings are considered.

The paper is organized as follows. In Section 2 we motivate further the need for improved models of void growth and coalescence by a set of finite-element calculations of voided unit-cells subject to imposed stress histories. Next, we recall the variational formulation of the effective yield criterion in Section 3. In Section 4 the micromechanics problem is posed by specifying geometry, microscopic plasticity model and velocity fields. Section 5 is a self-contained derivation of the approximate effective yield function with details deferred to four appendices. In the following section, salient features of the derived yield surfaces are analyzed using data for three orthotropic materials. We close the model equations by developing laws for microstructure evolution in Section 7 along with some preliminary, but discriminating, comparisons with finite element calculations of voided cells.

2 Finite Element Simulations

We present a set of finite element calculations on porous representative volume elements (RVE) to demonstrate the subtle coupling between the effects of void shape and material

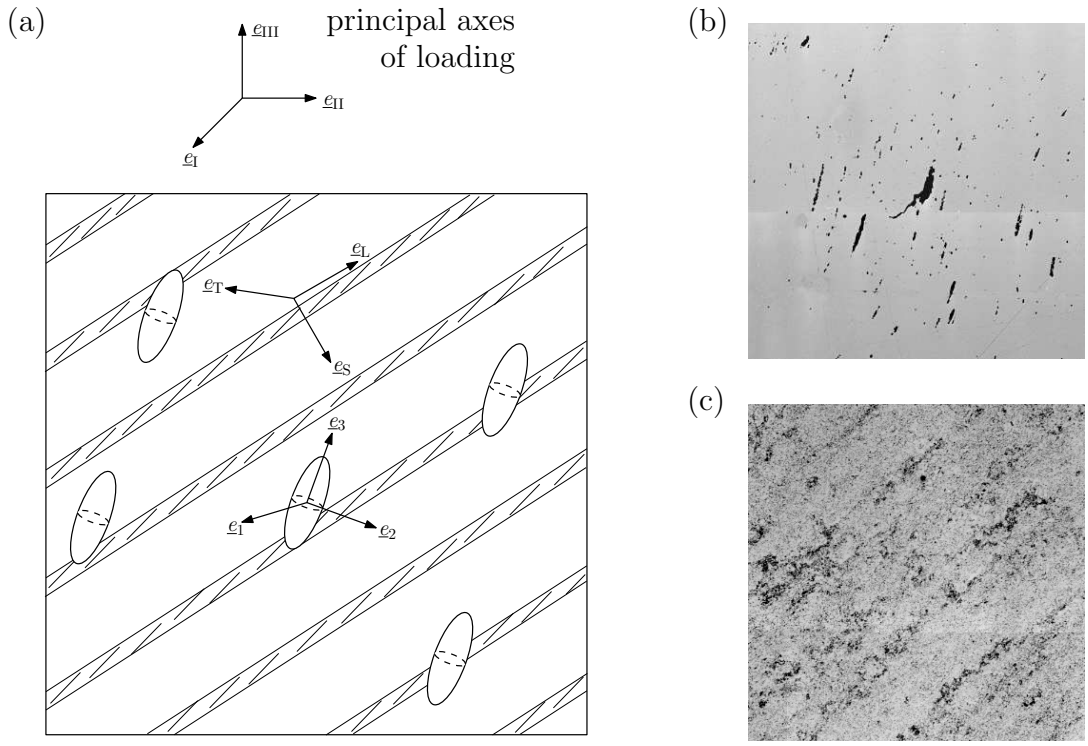

Figure 2: (a) Sketch of porous material consisting of an aggregate of aligned spheroidal voids embedded in a plastically orthotropic matrix. (b) Actual configuration of void population in an initially dense steel after heavy deformation under off-axes triaxial loading (Benzerga, 2000). (c) Etched cross-section of same specimen revealing its two-phase microstructure, ferrite (bright phase) and banded pearlite responsible for plastic anisotropy (dark phase). Orientation of void aggregate in (b) is not that of pearlite bands in (c) because of deformation-induced anisotropy.

anisotropy and motivate the need for an improved model. In all simulations, the principal axes of the void, the axes of material orthotropy and the principal axes of the loading all coincide. Thus, the chosen configuration is considerably simplified from the general case sketched in Fig. 2. Yet, it illustrates important points while allowing for the analysis to be conducted under axisymmetric conditions.

The calculations are based on the concept of a unit-cell containing a void as elaborated upon by Tvergaard (1982) and further developed by Koplik and Needleman (1988). A spheroidal void is embedded in an elastoplastic cylindrical matrix, as sketched in Fig. 3, with elastic constants $E = 210$ GPa and $\nu = 0.3$. The geometry of the unit-cell is characterized by the initial porosity, f_0, void aspect ratio, w_0, defined as the ratio of the axial to transverse semi-axes, and the cell aspect ratio, H_0/R_0. Invariance of material plastic flow properties about an axis $\underline{e}_{\mathrm{S}}$ is assumed. The latter is identified with the axis of the spheroidal void $\underline{e}_3$. The hatched bands in Fig. 3a schematically represent pearlite banding as in Fig. 2 and, more generally, any processing-induced texturing of the matrix material. More specifically, the matrix is taken to be plastically anisotropic of the Hill type, with the associated flow rule and power-law strain-hardening of the form $\bar{\sigma} = \sigma_{\mathrm{S}}(1 + \bar{\epsilon}/\epsilon_0)^N$, where $\bar{\sigma}$ and $\bar{\epsilon}$ are work-conjugate measures of matrix effective stress and plastic strain, respectively. To avoid confusion with the notion of *effective* properties, we will refer to $\bar{\epsilon}$ as the cumulative plastic strain. Here, $\epsilon_0 = 0.002$ is a constant strain

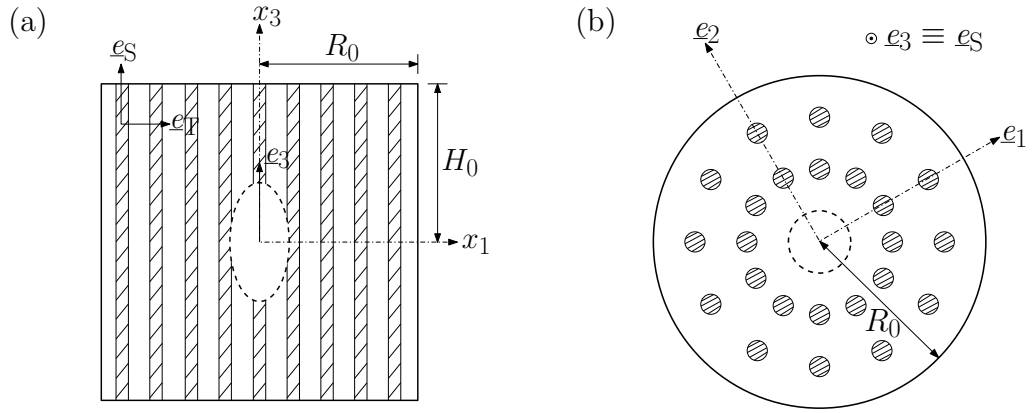

Figure 3: Configuration of the cylindrical RVE considered in the finite element simulations. (a) Front view. (b) Top view. Void axis $\underline{e}_3$ and axis of transverse isotropy $\underline{e}_S$ are the same.

offset, $N = 0.1$ is the hardening exponent and $\sigma_S = 420$ MPa is the initial yield stress of the matrix material along $\underline{e}_S$. The applied loading is taken to be axially symmetric about $\underline{e}_3$.

The computations are carried out using the object-oriented finite-element (FE) code ZeBuLoN (Besson and Foerch, 1997) and a Lagrangian formulation of the field equations. The cell boundaries are constrained to remain straight so that the unit cell is representative of a periodic array of voids. Special boundary conditions are formulated such that, in any given calculation, the ratio γ of net axial stress, Σ_{33}, to net lateral stress, Σ_{11}, remains constant throughout. Stress triaxiality is measured by the ratio T of mean normal stress, Σ_m, to the von Mises effective stress, Σ_e, given by:

$$\Sigma_e = |\Sigma_{33} - \Sigma_{11}|, \quad \Sigma_m = \frac{1}{3}(\Sigma_{33} + 2\Sigma_{11}), \quad T = \frac{\Sigma_m}{\Sigma_e} = \frac{1}{3}\frac{2\gamma + 1}{|1 - \gamma|} \tag{1}$$

A Riks algorithm (Riks, 1979) is used to integrate the nonlinear constitutive equations in order to keep the stress ratio γ, and hence T, constant. T is taken to be unity in the calculations presented here. The effective response of the unit cell is defined in terms of the effective stress Σ_e above versus an effective strain, E_e, defined as follows:

$$E_e = \frac{2}{3}|E_{33} - E_{11}|; \quad E_{33} = \ln\left(\frac{H}{H_0}\right), \quad E_{11} = \ln\left(\frac{R}{R_0}\right) \tag{2}$$

where H and R are the current height and radius of the cylindrical unit cell, respectively, and H_0 and R_0 their initial values (Fig. 3).

In all calculations, $H_0/R_0 = 1$, the initial void volume fraction is fixed at $f_0 = 0.001$ while three values of the void aspect ratio are used: $w_0 = 1/2$ (oblate void), $w_0 = 1$ (spherical void) and $w_0 = 2$ (prolate void). Typical meshes are shown in Fig. 4, which consist of sub-integrated quadratic quadrilateral elements. Exploiting the symmetry of the problem, only one fourth of the domain is meshed. All material parameters are kept fixed except w_0 and the Hill anisotropy factors that characterize plastic flow in the matrix. Two sets of Hill coefficients are used which are representative of an aluminum alloy and a zirconium alloy and referred to as Material 1 and Material 2, respectively (Table 1). The third set of values (Material 3) will be used later. In a reference calculation, the material is isotropic and the void spherical ($w_0 = 1$).

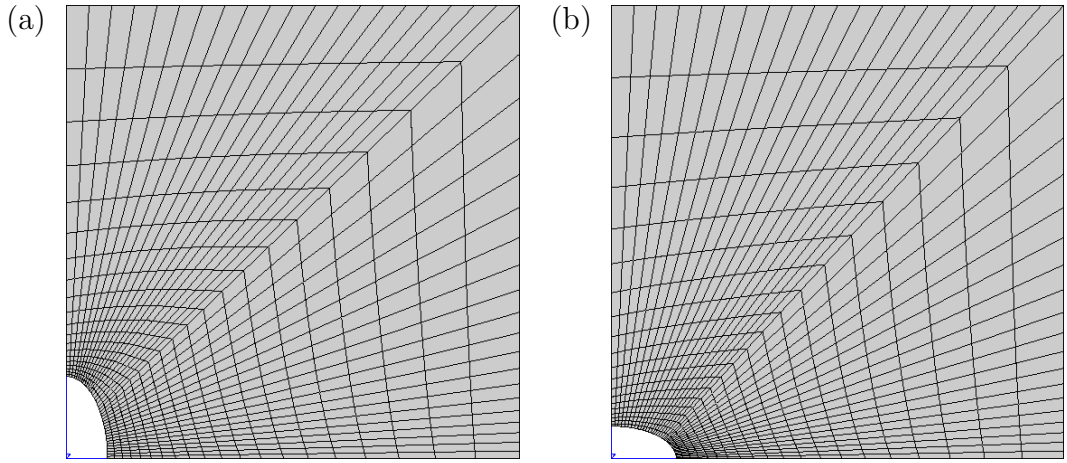

Figure 4: Finite element meshes used in the unit-cell calculations with initial porosity $f_0 = 0.001$, cell aspect ratio $H_0/R_0 = 1$, and void aspect ratio (a) $w_0 = 2$, and (b) $w_0 = 1/2$.

	h_{L}	h_{T}	h_{S}	h_{TS}	h_{SL}	h_{LT}
Isotropic	1.000	1.000	1.000	1.000	1.000	1.000
Material 1	1.000	1.000	1.000	2.333	2.333	1.000
Material 2	1.000	1.000	1.000	0.500	0.500	1.000
Material 3	1.650	0.778	0.893	1.378	0.943	1.627

Table 1: Matrix material anisotropy parameters, h_i, used in the numerical computations. h_i ($i = \mathrm{L}, \mathrm{T}, \mathrm{S}, \mathrm{TS}, \mathrm{SL}, \mathrm{LT}$) represent the diagonal elements of the Voigt representation of Hill's tensor in deviatoric stress space, $\mathbb{h}$, expressed in the frame of material orthotropy; see Section 4.2 for details.

The effective responses of the anisotropic unit cells are compared in Fig. 5a with that of an isotropic solid (i.e., isotropic matrix and $w_0 = 1$). The effective stress is normalized by the matrix yield stress σ_{S}. The corresponding porosity versus effective strain curves are shown in Fig. 5b. The calculations, which were terminated just at the onset of void coalescence, illustrate three typical trends. First, the effect of initial void aspect ratio w_0 is generally significant: in Material 1 there is nearly a 0.25 difference in effective strain between the $w_0 = 1/2$ and $w_0 = 2$ cases at incipient void coalescence. This result demonstrates the effect of initial void shape on void growth rates, in keeping with previous studies (Pardoen and Hutchinson, 2000). Next, at fixed value of w_0, changing the matrix anisotropy properties from Material 1 to Material 2 drastically affects the stress bearing capacity of the unit cell (Fig. 5a) as well as the rate of increase of porosity (Fig. 5b) with the effect being more dramatic for the oblate void ($w_0 = 1/2$). Finally, the combined effect of plastic anisotropy and void shape can yield unexpected trends as is the case for Material 2: the effect of initial void shape, which is invariably present in isotropic matrices, simply disappears within the range of w_0 considered here (Fig. 5). For reference, the results corresponding to the isotropic matrix with $w_0 = 1/2$ and $w_0 = 2$ fall in between the results for materials 1 and 2. They are not shown in Fig. 5 for the sake of clarity.

None of the available porous plasticity models capture all aspects of the behavior documented in Fig. 5. This includes the heuristic model of Benzerga et al. (2004) who

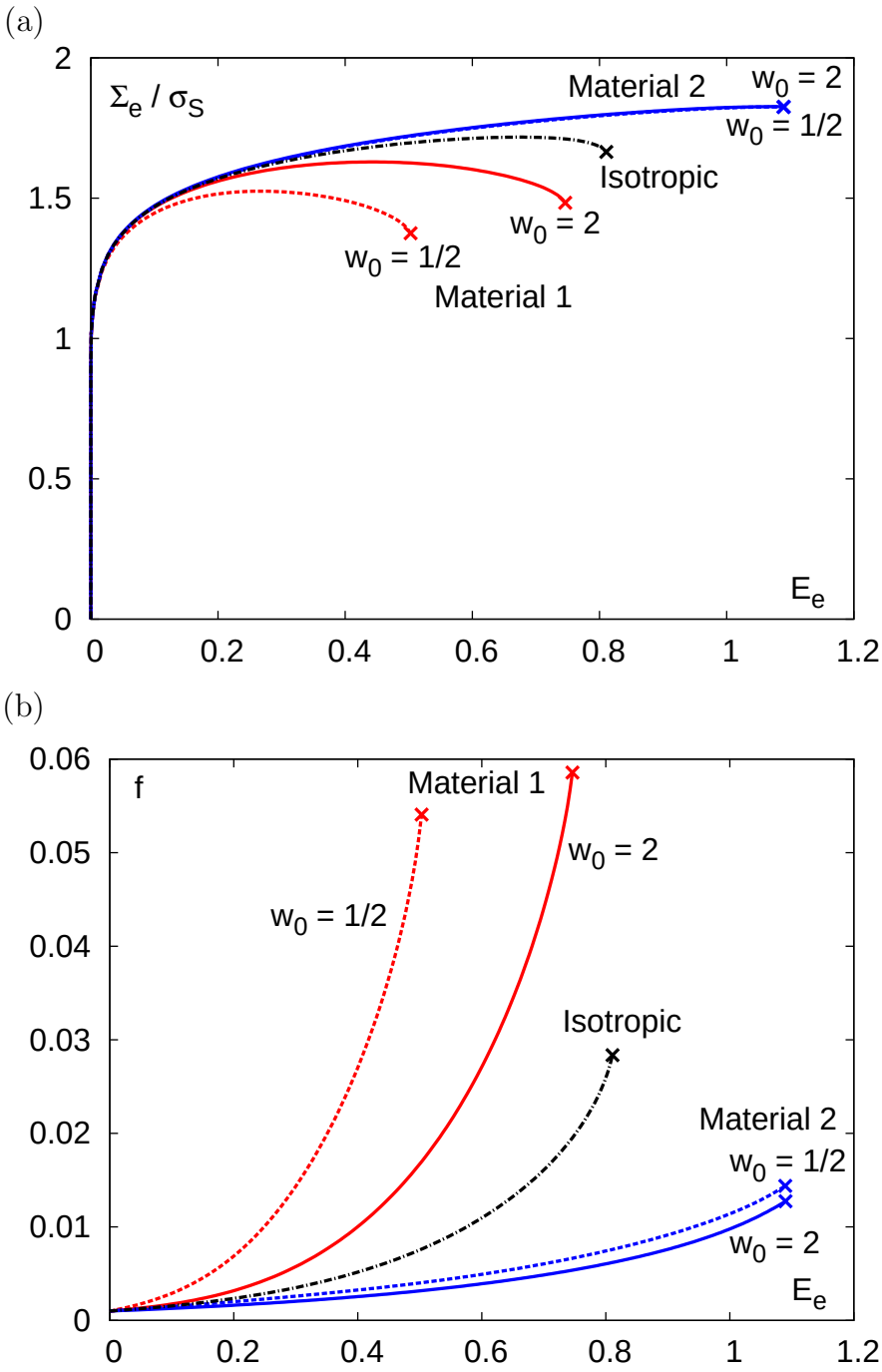

Figure 5: Results of unit-cell calculations for two transversely isotropic matrix materials (Table 1) containing either oblate ($w_0 = 1/2$) or prolate ($w_0 = 2$) voids. (a) Effective stress, Σ_e, normalized by the matrix yield stress in tension along $\underline{e}_S$, versus effective strain, E_e. (b) void volume fraction versus E_e. Key data include: initial porosity $f_0 = 0.001$; matrix hardening exponent $N = 0.1$; and stress triaxiality ratio $T = 1$. For comparison, results for initially spherical void in an isotropic matrix are also shown.

conjectured that the combined effect of void shape and plastic anisotropy is a simple superposition of separate effects. In fact, the effect of plastic anisotropy is more subtle than discussed above. Examination of the deformed configurations for an initially prolate cavity, Fig. 6a-c, shows that void growth depends on material anisotropy even when the void aspect ratio evolves in a nearly identical fashion (Fig. 6d). As previously shown in Fig. 5b, the porosity grows much faster in Material 1 than in Material 2 leading to a much lower ductility for the former. This is in contrast with existing void growth models (Gologanu et al., 1997; Benzerga, 2000; Pardoen and Hutchinson, 2000), which would predict nearly identical evolutions of the porosity in these two materials.

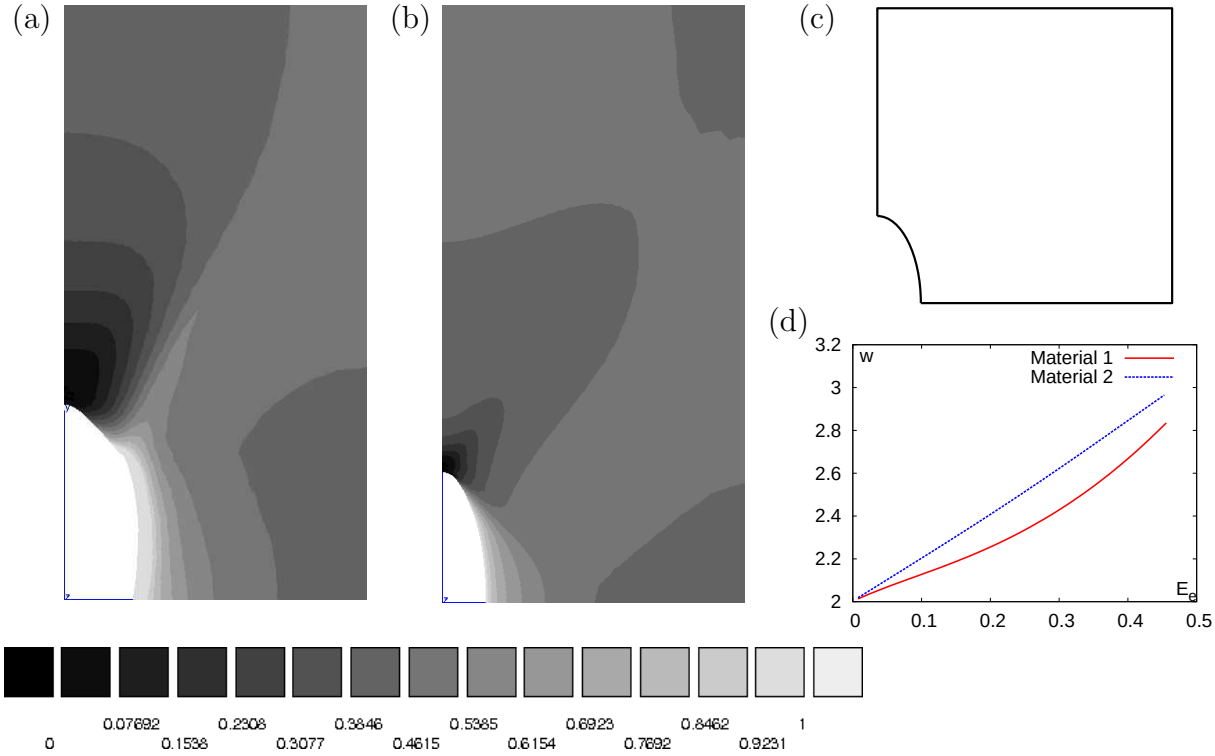

Figure 6: Contours of cumulative plastic strain, $\bar{\epsilon}$, at a unit cell effective strain $E_e = 0.45$ and $T = 1$ using $f_0 = 0.001$, $w_0 = 2$, $H_0/R_0 = 1$, $N = 0.1$ and anisotropy parameters for (a) Material 1; and (b) Material 2 from Table 1. (c) Initial state. (d) Evolution of void aspect ratio w. Nearly identical evolutions of void aspect ratio do not necessarily imply the same amount of void enlargement.

In fact, the strong coupling between plastic anisotropy and void shape effects is not surprising. Void growth is merely the expression of plastic deformation of the surrounding matrix. Physically, it is therefore expected that the ease, or difficulty, with which plastic flow takes place in the matrix will affect the rate of void growth. While the results in Figs. 5–6 provide a quantification of this coupling, it remains that such results hold for particular choices made for the initial microstructural parameters, loading history, etc. One can only carry out a finite number of such unit cell calculations. A more challenging task is to derive a mathematical plasticity model with an inherent predictive capability of coupled anisotropy effects as evidenced at the mesoscopic, unit-cell level. In doing so, the ambition goes beyond the restrictive case of transversely isotropic matrices and axisymmetric proportional loadings. On the other hand, derivation of such a mathematical

model from first principles is currently not tractable without some basic restrictions. Chief among these are the neglect of elasticity and work hardening in the matrix material. In return, the derivation can be tackled using tools and concepts from limit analysis and nonlinear homogenization theory.

3 Variational Formulation of the Yield Criterion

The effective yield criterion of a porous anisotropic material is determined through homogenization of a representative volume element occupying domain Ω and containing voids that jointly occupy sub-domain ω. The kinematic approach of Hill–Mandel homogenization theory (Hill, 1967; Mandel, 1964) is used, wherein the RVE is subjected to uniform deformation-rate boundary conditions, i.e.,

$$v_i = D_{ij} x_j \qquad \text{on} \quad \partial\Omega \tag{3}$$

where $\underline{v}$ is the microscopic velocity field and $\mathbf{D}$ is a second-rank symmetric tensor, which specifies the loading. It is straightforward to show that the imposed boundary rate of deformation, $\mathbf{D}$, is equal to the volume average of the microscopic rate of deformation, $\mathbf{d}$, over the volume of the RVE. The corresponding macroscopic stress, $\mathbf{\Sigma}$, is defined in an analogous way as the volume average over Ω of the microscopic Cauchy stress, $\boldsymbol{\sigma}$. Hence,

$$D_{ij} = \langle d_{ij} \rangle_\Omega, \qquad \Sigma_{ij} \equiv \langle \sigma_{ij} \rangle_\Omega, \tag{4}$$

where the notation $\langle \cdot \rangle_\Omega$ is for volume averaging over Ω. For a porous material, (4) remains valid regardless of the extensions chosen for the fields $\boldsymbol{\sigma}$ and $\mathbf{d}$ within the void, provided that the boundary of the void remains traction free and the velocity field is continuous across the boundary. The Hill–Mandel lemma (Hill, 1967; Mandel, 1964) entails that the above defined macroscopic measures of stress and rate of deformation are work conjugate. It may be noted that in the lemma $\boldsymbol{\sigma}$ and $\mathbf{d}$ need not be related through a constitutive relation. For a rigid perfectly plastic matrix material with normality obeyed, the macroscopic, or effective, yield surface in stress space is determined using the classical limit-analysis theorem identifying the sets of potentially and actually sustainable loads (Suquet, 1982), and is defined by

$$\Sigma_{ij} = \frac{\partial \Pi}{\partial D_{ij}}(\mathbf{D}) \tag{5}$$

Here, $\Pi(\mathbf{D})$ is the macroscopic plastic dissipation defined as the infimum of the volume-average of the microscopic plastic dissipation $\pi(\mathbf{d})$, the infimum being calculated over all admissible microscopic deformation fields. The above theorem and equation (5) also apply when elasticity is included if transformations are small. Physically, equation (5) means that among all microscopic diffuse modes of plastic deformation, those that result in the smallest average dissipation over the cell will define "macroscopic" yielding. Formally,

$$\Pi(\mathbf{D}) = \inf_{\mathbf{d} \in \mathcal{K}(\mathbf{D})} \langle \pi(\mathbf{d}) \rangle_\Omega \tag{6}$$

where $\mathcal{K}(\mathbf{D})$ denotes the set of kinematically admissible microscopic deformations:

$$\mathcal{K}(\mathbf{D}) = \{\mathbf{d} | \exists \underline{v}, \forall \underline{x} \in \Omega,\ d_{ij} = \frac{1}{2}(v_{i,j} + v_{j,i}) \text{ and } \forall \underline{x} \in \partial\Omega,\ v_i = D_{ij} x_j\} \tag{7}$$

For a given deviator $\mathbf{d}$, the microscopic plastic dissipation is defined as

$$\pi(\mathbf{d}) = \sup_{\boldsymbol{\sigma}^* \in \mathcal{C}} \sigma^*_{ij}\, d_{ij} \tag{8}$$

the supremum being taken over all microscopic stresses that fall within the microscopic convex $\mathcal{C}$ of elasticity.

Equations (5) through (8) represent a variational definition of the effective yield criterion. Actual derivation of the latter requires that the following be specified: (i) the geometry of the RVE; (ii) a micro-scale plasticity model, which enters through the term $\pi(\mathbf{d})$; and (iii) trial velocity fields defining the set $\mathcal{K}(\mathbf{D})$ for use in (6). These tasks are undertaken in the following section.

4 Problem Definition

Using the variational approach above, an effective yield criterion is sought for anisotropic porous materials subjected to arbitrary loadings. Aligned spheroidal voids are embedded in a rigid, plastically orthotropic matrix. Elasticity is thus neglected in the analysis so that (5) applies at finite strains. It will be included heuristically at the end within a hypoelastic framework. The microstructure orientation is defined by two triads: (i) $(\underline{e}_1, \underline{e}_2, \underline{e}_3)$ associated with the aggregate of spheroidal voids with $\underline{e}_3$ being their common axis and $\underline{e}_1, \underline{e}_2$ chosen arbitrarily; and (ii) $(\underline{e}_{\rm L}, \underline{e}_{\rm T}, \underline{e}_{\rm S})$ associated with the directions of orthotropy of the matrix. The microstructural and matrix triads are not necessarily tied to each other; see Fig. 2a. Under an arbitrary macroscopic stress state with principal axes $(\underline{e}_{\rm I}, \underline{e}_{\rm II}, \underline{e}_{\rm III})$, initially spheroidal voids would develop into three-dimensional voids. This evolution is neglected in the present treatment:

Approximation $\mathcal{A}_1$: We approximate the void shape to be spheroidal at every stage of the deformation.

This approximation is similar to Gurson's assumption of spherical voids in his derivation of the isotropic criterion. It can be further justified on the basis that the objective is to develop an accurate estimate of the macroscopic yield criterion, not to determine the exact microscopic fields. Finding the latter is a challenging problem because of their expected dependence upon specific matrix flow characteristics and of other subtle nonlinear effects[1]. The microscopic velocity fields are important, however, in determining the evolution laws for some microstructural variables. The treatment of the evolution problem in Section 7, therefore, will examine possible strategies to correct for the inaccuracies in the assumed velocity fields.

It is worth noting that while the homogenization procedure outlined in Section 3 is more easily tractable for spheroidal void shapes, alternative homogenization approaches using non-linear extensions of the Hashin-Shtrikman theory (Ponte Castaneda, 1991) have been effectively used for ellipsoidal void geometries. While earlier versions of such models (Ponte Castañeda and Zaidman, 1994; Kailasam and Ponte Castaneda, 1998) did not provide good agreement with numerical estimates of the yield criterion at high stress triaxialities, recent extensions based on a second order homogenization procedure (Danas and

[1] A typical example is the counterintuitive flattening of cavities under axial loading with sufficient amount of superposed hydrostatic stress.

Ponte Castañeda, 2009) provide approximate, but more accurate results. However, these models have not yet been extended to treat the case of plastically anisotropic matrices. In passing, we also note a recent formulation of admissible velocity fields by Leblond and Gologanu (2008) for ellipsoidal voids. It remains to be seen whether the homogenization procedure of Section 3 is tractable in that case.

4.1 Geometry and Coordinates

Following previous works on void shape effects (Gologanu et al., 1993, 1994, 1997), we consider a spheroidal RVE containing a confocal spheroidal void, as shown in Fig. 7. Let a

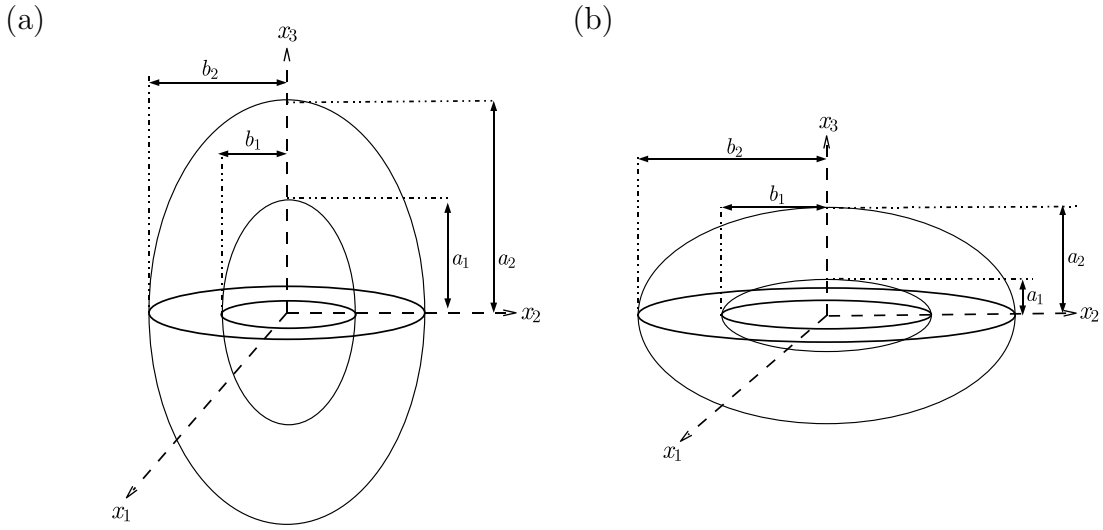

Figure 7: Porous representative volume elements used in the derivation of the analytical yield criterion. The cases of prolate (a), and oblate (b) voids require separate treatments.

and b represent respectively the lengths of the axial and transverse semi-axes of the current confocal spheroid, and let $c = \sqrt{|a^2 - b^2|}$ represent the semi-focal length. Hereafter, the subscripts 1 and 2 shall represent variable values at the void and RVE boundaries, respectively. At fixed void orientation, the geometry is thus completely defined by two dimensionless parameters; the porosity, $f = |\omega|/|\Omega| = a_1 b_1^2 / a_2 b_2^2$, and the void aspect ratio, $w \equiv a_1/b_1$. For given values of f and w, the eccentricities of the inner and outer spheroids may be uniquely determined from the relations

$$e_1^2 = \begin{cases} 1 - \dfrac{1}{w^2} & \text{(p)} \\ 1 - w^2 & \text{(o)} \end{cases}, \qquad \frac{(1-e_2^2)^n}{e_2^3} = \frac{1}{f}\frac{(1-e_1^2)^n}{e_1^3}, \qquad n = \begin{cases} 1 & \text{(p)} \\ 1/2 & \text{(o)} \end{cases} \tag{9}$$

where the shorthand notations (p) and (o) stand for prolate and oblate, respectively.

Due to the chosen geometry of the RVEs, we shall mainly employ the spheroidal coordinate system $(\lambda, \beta, \varphi)$ for the subsequent analysis. The base vectors of the spheroidal frame are defined by

$$\begin{aligned} \underline{e}_\lambda &= \{a \sin\beta \cos\varphi \underline{e}_1 + a \sin\beta \sin\varphi \underline{e}_2 + b \cos\beta \underline{e}_3\}/\sqrt{g_{\lambda\lambda}} \\ \underline{e}_\beta &= \{b \cos\beta \cos\varphi \underline{e}_1 + b \cos\beta \sin\varphi \underline{e}_2 - a \sin\beta \underline{e}_3\}/\sqrt{g_{\lambda\lambda}} \\ \underline{e}_\varphi &= -\sin\varphi \underline{e}_1 + \cos\varphi \underline{e}_2 \end{aligned} \tag{10}$$

$$g_{\lambda\lambda} \equiv a^2 \sin^2\beta + b^2 \cos^2\beta, \qquad \begin{cases} a = c\cosh\lambda,\ b = c\sinh\lambda & \text{(p)} \\ a = c\sinh\lambda,\ b = c\cosh\lambda & \text{(o)} \end{cases} \tag{11}$$

where $(\underline{e}_1, \underline{e}_2, \underline{e}_3)$ is the Cartesian base associated with the voids introduced above (also see Fig. 2c). With this choice of coordinates, the boundaries of the void and the RVE correspond to constant values of λ, designated λ_1 and λ_2 respectively. The eccentricity of the current confocal spheroid, e, is related to λ by the relation $e = 1/\cosh\lambda$.

4.2 Microscale Plasticity Model

The RVE is assumed to be made of a rigid ideal plastic orthotropic and incompressible material obeying the Hill quadratic yield criterion (Hill, 1948), which writes

$$\sigma_{\text{eq}} \equiv \sqrt{\frac{3}{2}\boldsymbol{\sigma} : \mathbb{p} : \boldsymbol{\sigma}} = \sqrt{\frac{3}{2}\boldsymbol{\sigma}' : \mathbb{h} : \boldsymbol{\sigma}'} \leq \bar{\sigma}, \qquad \mathbb{p} = \mathbb{J} : \mathbb{h} : \mathbb{J} \tag{12}$$

where the prime denotes the deviatoric part of a second order tensor and $\bar{\sigma}$ is the yield stress of the material in a reference direction. The fourth order tensor $\mathbb{p}$ denotes the Hill anisotropy tensor, $\mathbb{h}$ denotes the anisotropy tensor in the deviatoric stress space and $\mathbb{J}$ denotes the deviatoric projection operator defined by $\mathbb{J} \equiv \mathbb{I} - \frac{1}{3}\mathbf{I}\otimes\mathbf{I}$, where $\mathbb{I}$ and $\mathbf{I}$ are the fourth and second order identity tensors, respectively. The symbol $\otimes$ denotes the dyadic product, defined by $(\mathbf{I}\otimes\mathbf{I})_{ijkl} \equiv I_{ij}I_{kl}$. Typically, $\bar{\sigma}$ is chosen as the yield stress in one of the directions of orthotropy of the matrix material and the components of the anisotropy tensors $\mathbb{p}$ and $\mathbb{h}$ in (12) are scaled accordingly. The material obeys the associated flow rule, which may be written in the following form

$$\mathbf{d} = \frac{3}{2}\frac{d_{\text{eq}}}{\bar{\sigma}}\mathbb{p} : \boldsymbol{\sigma} \tag{13}$$

where d_{eq} is defined work-conjugate to σ_{eq} as the equivalent microscopic strain rate

$$d_{\text{eq}} = \sqrt{\frac{2}{3}\mathbf{d} : \hat{\mathbb{h}} : \mathbf{d}} \tag{14}$$

Here, $\hat{\mathbb{h}}$ is a formal inverse of tensor $\mathbb{h}$. It is defined by Benzerga and Besson (2001) as

$$\hat{\mathbb{p}} \equiv \mathbb{J} : \hat{\mathbb{h}} : \mathbb{J}, \qquad \mathbb{p} : \hat{\mathbb{p}} = \hat{\mathbb{p}} : \mathbb{p} = \mathbb{J} \tag{15}$$

Both $\mathbb{h}$ and $\hat{\mathbb{h}}$ are symmetric positive definite tensors; i.e. $h_{ijkl} = h_{jikl} = h_{ijlk} = h_{klij}$ and $\forall\boldsymbol{\sigma} \neq \mathbf{0},\ \boldsymbol{\sigma} : \mathbb{h} : \boldsymbol{\sigma} > 0$. In the frame of material orthotropy (Fig. 2), $\mathbb{h}$ and $\hat{\mathbb{h}}$ may be expressed as diagonal 6×6 matrices using Voigt's condensation. The six Hill coefficients are then denoted h_{L}, h_{T}, etc. (see Table 1). For a Hill material with associated flow rule, the microscopic plastic dissipation in (8) takes the form

$$\pi(\mathbf{d}) = \begin{cases} \bar{\sigma}\, d_{\text{eq}} & \text{(in the matrix)} \\ 0 & \text{(in the voids)} \end{cases} \tag{16}$$

4.3 Microscopic Velocity Fields

To describe plastic flow in the matrix, the velocity field is taken as a linear combination of two incompressible trial velocity fields

$$\forall \underline{x} \in \Omega \backslash \omega, \quad v_i(\underline{x}) = A v_i^A(\underline{x}) + \beta_{ij} x_j, \tag{17}$$

where scalar A and tensor $\boldsymbol{\beta}$ are parameters. Thus, $\underline{v}$ leads to an inhomogeneous deformation field, $\mathbf{d}^A$, responsible for void expansion, and a homogeneous field $\boldsymbol{\beta}$. Matrix incompressibility requires that the latter be a pure deviator ($\beta_{kk} = 0$). The above decomposition was also used in previous works (Gurson, 1977; Gologanu et al., 1997; Benzerga and Besson, 2001; Monchiet et al., 2008). Here, however, the homogeneous part $\boldsymbol{\beta}$ is not required to be axisymmetric. The expansion velocity field, $\underline{v}^A$, is taken to be axisymmetric about the void axis and constructed from the family of incompressible velocity fields introduced by Lee and Mear (1992). Its components in spheroidal coordinates are:

$$\left\{ \begin{array}{l} v_\lambda(\lambda,\beta) = c^2/\sqrt{g_{\lambda\lambda}}\,\{B_{00}/\sinh(\lambda) \\ \quad + \displaystyle\sum_{k=2,4,..}^{+\infty}\sum_{m=0}^{+\infty} k(k+1)[B_{km}Q_m^1(\zeta) + C_{km}P_m^1(\zeta)]P_k(\xi)\} \\ \qquad\qquad\qquad\qquad\qquad\qquad\qquad\qquad\qquad\qquad\qquad\qquad\qquad\qquad \text{(p)} \\ v_\beta(\lambda,\beta) = c^2/\sqrt{g_{\lambda\lambda}}\,\{\displaystyle\sum_{k=2,4,..}^{+\infty}\sum_{m=1}^{+\infty} m(m+1)[B_{km}Q_m(\zeta) \\ \qquad\qquad\qquad\qquad\qquad\qquad\qquad\qquad +C_{km}P_m(\zeta)]P_k^1(\xi)\} \end{array} \right. \tag{18}$$

$$\left\{ \begin{array}{l} v_\lambda(\lambda,\beta) = c^2/\sqrt{g_{\lambda\lambda}}\,\{B_{00}/\cosh(\lambda) \\ \quad + \displaystyle\sum_{k=2,4,..}^{+\infty}\sum_{m=0}^{+\infty} k(k+1)i^m[i\,B_{km}Q_m^1(\zeta) + C_{km}P_m^1(\zeta)]P_k(\xi)\} \\ \qquad\qquad\qquad\qquad\qquad\qquad\qquad\qquad\qquad\qquad\qquad\qquad\qquad\qquad \text{(o)} \\ v_\beta(\lambda,\beta) = c^2/\sqrt{g_{\lambda\lambda}}\,\{\displaystyle\sum_{k=2,4,..}^{+\infty}\sum_{m=1}^{+\infty} m(m+1)i^m[i\,B_{km}Q_m(\zeta) \\ \qquad\qquad\qquad\qquad\qquad\qquad\qquad\qquad +C_{km}P_m(\zeta)]P_k^1(\xi)\} \end{array} \right. \tag{19}$$

where

$$\zeta \equiv \left\{ \begin{array}{ll} \cosh\lambda & \text{(p)} \\ i\,\sinh\lambda & \text{(o)} \end{array} \right. ; \qquad \xi \equiv \cos\beta \tag{20}$$

In the above expressions, P_n^m and Q_n^m represent associated Legendre functions of the first and second kinds respectively, of order m and degree n (Gradshteyn and Ryzhik, 1980), B_{km} and C_{km} are arbitrary real constants and $i^2 = -1$.

As discussed by Gologanu et al. (1997), the condition of uniform boundary rate of deformation (3) formally fixes parameters A and $\boldsymbol{\beta}$ in a two-field approach such as (17). This may be seen by substituting the velocity field (17) into the macro-homogeneity condition $(4)_1$, which is itself a corollary of boundary condition (3); this yields:

$$D_{ij} = A\langle d_{ij}^A\rangle_\Omega + \beta_{ij} \tag{21}$$

Denoting $\mathbf{D}^A \equiv \langle \mathbf{d}^A\rangle_\Omega$ the contribution to $\mathbf{D}$ due to the expansion velocity field $\underline{v}^A$, it thus follows that parameters A and $\boldsymbol{\beta}$ are given by:

$$A = \frac{D_{\mathrm{m}}}{D_{\mathrm{m}}^A}, \quad \beta_{ij} = D_{ij} - \frac{D_{\mathrm{m}}}{D_{\mathrm{m}}^A} D_{ij}^A \tag{22}$$

where the subscript 'm' denotes the mean part of a tensor ($D_{\mathrm{m}} = D_{kk}/3$). Note that $\mathbf{D}^A$ is by definition axially symmetric about the void axis. In fact, the imposed boundary conditions imply further restrictions on the velocity fields. Since the second deformation field in (17) is uniform by construction, equation (3) also requires that:

$$v_i^A = D_{ij}^A \, x_j \qquad \text{for} \quad \lambda = \lambda_2 \tag{23}$$

This condition implies that coefficients B_{km} and C_{km} of the Lee–Mear fields (18)–(19) obey the following linear constraints (see Gologanu et al., 1997)

$$\begin{cases} e_2^3 B_{00}/(3(1-e_2^2)) + (3-e_2^2)F_2(\lambda_2)/\sqrt{1-e_2^2} - G_2(\lambda_2) = 0 & \text{(p)} \\ -e_2^3 B_{00}/(3\sqrt{1-e_2^2}) + (3-2e_2^2)F_2(\lambda_2)/\sqrt{1-e_2^2} - G_2(\lambda_2) = 0 & \text{(o)} \end{cases} \tag{24}$$

$$F_k(\lambda_2) = G_k(\lambda_2) = 0, \qquad k = 4, 6, 8... \tag{25}$$

where

$$\begin{cases} F_k(\lambda) \equiv \displaystyle\sum_{m=0}^{+\infty} \left[B_{km} Q_m^1(\zeta) + C_{km} P_m^1(\zeta) \right] \\ G_k(\lambda) \equiv \displaystyle\sum_{m=1}^{+\infty} m(m+1) \left[B_{km} Q_m(\zeta) + C_{km} P_m(\zeta) \right] \end{cases} \quad \text{(p)}$$

$$\begin{cases} F_k(\lambda) \equiv \displaystyle\sum_{m=0}^{+\infty} i^m \left[i B_{km} Q_m^1(\zeta) + C_{km} P_m^1(\zeta) \right] \\ G_k(\lambda) \equiv \displaystyle\sum_{m=1}^{+\infty} m(m+1) i^m \left[i B_{km} Q_m(\zeta) + C_{km} P_m(\zeta) \right] \end{cases} \quad \text{(o)} \tag{26}$$

In the derivation of the effective yield criterion in closed form, only four terms in the Lee–Mear expansion are used. These correspond to factors B_{00}, B_{20}, B_{21} and B_{22}. Since the field $\underline{v}^A$ is defined only up to a multiplicative constant, coefficient B_{00} is taken as unity to normalize the field and the remaining factors are collectively referred to as B_{2m} ($m = 0, 1, 2$). In the case of a spherical cavity, the fields related to the B_{2m} factors vanish and that related to B_{00} becomes spherically symmetric. The velocity fields corresponding to the coefficients C_{km} are not used since these fields do not vanish at infinity as is required, so that one can recover the correct limit behavior for a vanishingly small value of the porosity. The chosen velocity fields are in fact identical to those used by Gologanu et al. (1997) in their work on void shape effects and is a generalization of the fields used in the earlier works of Gologanu et al. (1993, 1994) (B_{00} and B_{22}) and Garajeu et al. (2000) (B_{00} and B_{20}). Recent work by Monchiet et al. (2008) using the Hill matrix also considered the fields B_{00} and B_{22} to describe the expansion field. However, we have chosen to use the above four fields to describe cavity expansion as this was found to yield a better correspondence with numerical estimates of the true yield criterion (Keralavarma, 2008; Keralavarma and Benzerga, 2008). In the case of isotropic matrices, comparison between the model developed by Gologanu et al. (1997) using four fields and their earlier models using two fields has evidenced superior predictive capability of the former regarding the evolution of microstructure.

5 Approximate Analytical Yield Criterion

The macroscopic yield locus is given by the parametric equation (5) with the dissipation function rewritten as:

$$\Pi(\mathbf{D}) = \inf_{\mathbf{d}\in\mathcal{K}(\mathbf{D})} \langle \sup_{\boldsymbol{\sigma}^*\in\mathcal{C}} \sigma^*_{ij}\, d_{ij} \rangle_\Omega \tag{27}$$

With the choice (12)–(13) made for the matrix plasticity model and the choice (17)–(19) for the microscopic velocity fields, an estimate of $\Pi(\mathbf{D})$ is, in view of (16),

$$\Pi(\mathbf{D}) = \bar{\sigma}(1-f)\langle d_{\rm eq}\rangle_{\Omega\setminus\omega} = \frac{\bar{\sigma}}{\Omega}\int_{\lambda_1}^{\lambda_2}\int_0^{\pi}\int_0^{2\pi} d_{\rm eq} b\, g_{\lambda\lambda}\, \sin\beta\, d\varphi\, d\beta\, d\lambda \tag{28}$$

In this expression, $d_{\rm eq}$, which is defined by (14), is evaluated for the specific set of chosen admissible velocity fields. Since a subset of $\mathcal{K}(\mathbf{D})$ is used, Eq. (28) delivers an upper bound for the true dissipation. For notational convenience, this upper-bound value and other subsequent estimates are also designated $\Pi(\mathbf{D})$. As noted above, imposition of kinematic boundary conditions in terms of $\mathbf{D}$ formally determines the velocity field through (22) thus eliminating the need for explicit minimization in computing the macroscopic plastic dissipation, Eq. (27). However, the coefficients B_{km} appearing in the expression of $\underline{v}^A$ are left undefined, to be fixed later independently of the boundary conditions. Rewriting $d_{\rm eq}$ in terms of the fields $\mathbf{d}^A$ and $\boldsymbol{\beta}$, we get

$$d_{\rm eq} = \sqrt{A^2 d_{\rm eq}^{A^2} + {\beta_{\rm eq}}^2 + \frac{4}{3} A\mathbf{d}^A : \hat{\mathbb{h}} : \boldsymbol{\beta}} \tag{29}$$

Here and subsequently, the meaning of subscript "eq" is consistent with definition (14) for deformation related quantities. Now, let

$$\langle d_{\rm eq}\rangle_{(\beta,\varphi)} \equiv \frac{\int_0^{\pi}\int_0^{2\pi} d_{\rm eq} g_{\lambda\lambda}\, \sin\beta\, d\varphi\, d\beta}{\int_0^{\pi}\int_0^{2\pi} g_{\lambda\lambda}\, \sin\beta\, d\varphi\, d\beta} = \frac{3}{4\pi(2a^2+b^2)}\int_0^{\pi}\int_0^{2\pi} d_{\rm eq} g_{\lambda\lambda}\, \sin\beta\, d\varphi\, d\beta \tag{30}$$

be the average value of $d_{\rm eq}$ over coordinates β and φ. Then, using the change of variable $y = c^3/ab^2$, (28) becomes:

$$\Pi(\mathbf{D}) = \bar{\sigma} y_2 \int_{y_2}^{y_1} \langle d_{\rm eq}\rangle_{(\beta,\varphi)} \frac{dy}{y^2} \tag{31}$$

which can be rigorously bounded from above by

$$\Pi(\mathbf{D}) = \bar{\sigma} y_2 \int_{y_2}^{y_1} \langle d_{\rm eq}^2\rangle^{1/2}_{(\beta,\varphi)} \frac{dy}{y^2} \tag{32}$$

using Hölder's inequality. We recall that subscripts 1 and 2 in the bounds of the integral refer to the inner void surface and outer surface of the RVE, respectively. Note at this juncture that the above change of variable to y singles out the case of a spherical cavity (for which $c \to 0$). A special treatment in that case leads to the criterion developed by Benzerga and Besson (2001) since the velocity field $\underline{v}^A$ reduces to a spherically symmetric field. We shall seek to recover this special case as the limit of the final criterion when $y_2 \to 0$. Now, from (29) we have

$$\langle d_{\rm eq}^2\rangle_{(\beta,\varphi)} = A^2\langle d_{\rm eq}^{A^2}\rangle_{(\beta,\varphi)} + {\beta_{\rm eq}}^2 + \frac{4}{3} A\langle d_{33}^A\rangle_{(\beta,\varphi)} \mathbf{Q} : \hat{\mathbb{h}} : \boldsymbol{\beta} \tag{33}$$

with

$$\mathbf{Q} \equiv -\frac{1}{2}(\underline{e}_1 \otimes \underline{e}_1 + \underline{e}_2 \otimes \underline{e}_2) + \underline{e}_3 \otimes \underline{e}_3 \tag{34}$$

Exact integration of (32) with the integrand specified through (33) and (34) is ruled out due to the complexity of the expression for d^A_{eq}. Anticipating approximations to come, in the spirit of Gologanu et al. (1997), we define two new functions $F(u)$ and $G(u)$ through

$$\langle d^{A^2}_{\text{eq}} \rangle_{(\beta,\varphi)} = F^2(u)u^2, \qquad \langle d^A_{33} \rangle_{(\beta,\varphi)} = F(u)G(u)u^2, \qquad u \equiv \begin{cases} y & \text{(p)} \\ \frac{y}{y+1} & \text{(o)} \end{cases} \tag{35}$$

thus operating a change of the spatial variable from y to u. This change of variable leaves the form of the integral in (32) unchanged for both prolate and oblate cavities. After rearranging, $\langle d^2_{\text{eq}} \rangle_{(\beta,\varphi)}$ may be written as

$$\langle d^2_{\text{eq}} \rangle_{(\beta,\varphi)} = \left[A\frac{F(u)}{\sqrt{\hat{h}_q}}\mathbf{Q} + \sqrt{\hat{h}_q}G(u)\boldsymbol{\beta} \right]^2_{\text{eq}} u^2 + H^2(u){\beta_{\text{eq}}}^2, \qquad H^2(u) \equiv 1 - \hat{h}_q G^2(u)u^2 \tag{36}$$

See above for the meaning of subscript "eq" and $\hat{h}_q$ is defined by

$$\hat{h}_q \equiv \frac{2}{3}\mathbf{Q} : \hat{\mathbb{h}} : \mathbf{Q} = \frac{\hat{h}_{11} + \hat{h}_{22} + 4\hat{h}_{33} - 4\hat{h}_{23} - 4\hat{h}_{31} + 2\hat{h}_{12}}{6} \tag{37}$$

$\hat{h}_{ij}$ above denote the Voigt-condensed components of the fourth-order tensor $\hat{\mathbb{h}}$, expressed in the basis associated with the void, hence the appearance of terms h_{23} etc. Since $\mathbf{Q}$ is axially symmetric about $\underline{e}_3$, it is clear that $\hat{h}_q$ is invariant with respect to the choice of axes $\underline{e}_1$ and $\underline{e}_2$ in Fig. 2.

Approximation $\mathcal{A}_2$: We simplify the spatial fluctuations of the microscopic rate of deformation by replacing functions $F(u)$, $G(u)$ and $H(u)$ in (36) by constants that approximately realize the minimum overall dissipation under some particular loading paths.

This permits evaluation of integral (32) in closed form. The accuracy of $\mathcal{A}_2$ can readily be assessed using numerical integration as illustrated by Keralavarma and Benzerga (2008) for transversely isotropic materials under axisymmetric loadings. In general, however, $\mathcal{A}_2$ is an "uncontrolled" approximation in the sense that it does not necessarily preserve the upper-bound character of $\Pi(\mathbf{D})$ under all loading paths. In Appendix A we study the spatial fluctuations of the deformation to justify replacing $F(u)$, $G(u)$ and $H(u)$ by constants designated $\bar{F}, \bar{G}$ and $\bar{H}$, respectively. For a frozen microstructure, the value of $\bar{F}$ is chosen such that the analytical criterion yields a close approximation to the true yield criterion for purely hydrostatic loading, while $\bar{G}$ and $\bar{H}$ are chosen such that the analytical criterion provides a close match to the true yield criterion for purely deviatoric axisymmetric loading about the void axis. Here, by true yield locus we mean the locus defined by equations (5) and (28) evaluated using the four velocity fields chosen in Section 4.3 and determined numerically without approximations. The precise constants $\bar{F}$, $\bar{G}$ and $\bar{H}$ and their dependence upon f and w will be specified later.

Thus, substituting (36) in (32) in view of $\mathcal{A}_2$, we can write the plastic dissipation in the Gurson-like form

$$\Pi(\mathbf{D}) = \bar{\sigma} y_2 \int_{u_2}^{u_1} \sqrt{\tilde{A}^2_{\text{eq}} u^2 + \tilde{B}^2_{\text{eq}}} \frac{du}{u^2} \tag{38}$$

where $\tilde{\mathbf{A}}$ and $\tilde{\mathbf{B}}$ are traceless tensors defined by

$$\tilde{\mathbf{A}} \equiv A\frac{\bar{F}}{\sqrt{\hat{h}_q}}\mathbf{Q} + \sqrt{\hat{h}_q}\bar{G}\boldsymbol{\beta}, \qquad \tilde{\mathbf{B}} \equiv \bar{H}\boldsymbol{\beta} \tag{39}$$

To obtain the closed form expression of the macroscopic yield locus, the components of $\mathbf{D}$ are to be eliminated from the parametric equation (5). $\mathbf{D}$ enters implicitly the equation above through A and $\boldsymbol{\beta}$. In Appendix B we provide the key steps for partial elimination of the parameters, leading to the following equation for the yield locus

$$q_2 C\frac{3}{2}\frac{\boldsymbol{\Sigma}:\mathbb{H}:\boldsymbol{\Sigma}}{\bar{\sigma}^2} + 2(g+1)(g+f)\cosh\left(q_1\kappa\frac{\boldsymbol{\Sigma}:\mathbf{X}}{\bar{\sigma}}\right) - (g+1)^2 - (g+f)^2 = 0 \tag{40}$$

where

$$\mathbb{H} \equiv (\mathbb{I} + \eta(\mathbf{X}\otimes\mathbf{Q}):\hat{\mathbb{p}}):\mathbb{p}:(\mathbb{I} + \hat{\mathbb{p}}:(\eta\mathbf{Q}\otimes\mathbf{X})), \tag{41}$$

$$\mathbf{X} \equiv \alpha_2(\underline{e}_1\otimes\underline{e}_1 + \underline{e}_2\otimes\underline{e}_2) + (1-2\alpha_2)\underline{e}_3\otimes\underline{e}_3 \tag{42}$$

and q_1 and q_2 are scalar-valued functions of $\boldsymbol{\beta}/A$. For example,

$$q_1 = \sqrt{1 + R_{\text{eq}}^2/\hat{h}_q}; \qquad \mathbf{R} \equiv \frac{(\mathbf{Q}:\hat{\mathbb{p}}:\mathbf{Q})\boldsymbol{\beta}/A - (\mathbf{Q}:\hat{\mathbb{p}}:\boldsymbol{\beta}/A)\mathbf{Q}}{\frac{3}{2}\bar{F}/\bar{G} + \mathbf{Q}:\hat{\mathbb{p}}:\boldsymbol{\beta}/A} \tag{43}$$

Expressions of the criterion parameters C, g, κ, η and α_2 are given in Appendix C. They are tied to the constants involved in approximation $\mathcal{A}_2$ above, i.e., $\bar{F}$, $\bar{G}$ and $\bar{H}$ whose derivation is also given in Appendix C. Most parameters depend on the anisotropy tensor $\mathbb{h}$; all of them are implicit functions of microstructural variables f and w. The effect of void orientation enters the criterion through tensors $\mathbf{Q}$ and $\mathbf{X}$ defined by (34) and (42), respectively, while matrix anisotropy enters via tensors $\mathbb{h}$ and $\hat{\mathbb{h}}$. An important formal difference with the model of Benzerga and Besson (2001) is that the fourth order tensor $\mathbb{H}$, which may be termed the macroscopic plastic anisotropy tensor, is different from the microscopic anisotropy tensor $\mathbb{h}$. This difference stems from the fact that the expansion velocity field $\underline{v}^A$ used in the previous work was spherically symmetric, whereas that used now is not. In the limit of a spherical cavity, $q_1 \to 1$ and so does q_2. We thus check that the criterion does not depend on the void orientation (see Appendix B).

Finally, since the plastic dissipation $\Pi(\mathbf{D})$ is positively homogeneous of degree 1, elimination of the ratio $\boldsymbol{\beta}/A$, which appears through q_1 and q_2, from criterion (40) is possible, at least in principle. However, the resulting criterion would be unnecessarily complicated. For the sake of simplicity, therefore, we adopt the final approximation as follows

Approximation $\mathcal{A}_3$: The derived yield criterion is approximated by replacing the coefficients q_1 and q_2 by unity in equation (40).

In Appendix D we provide some arguments pleading in favor of this approximation. The final form of the derived anisotropic yield criterion is thus written as $\mathcal{F}(\boldsymbol{\Sigma}) = 0$ with

$$\mathcal{F}(\boldsymbol{\Sigma}) = C\frac{3}{2}\frac{\boldsymbol{\Sigma}:\mathbb{H}:\boldsymbol{\Sigma}}{\bar{\sigma}^2} + 2(g+1)(g+f)\cosh\left(\kappa\frac{\boldsymbol{\Sigma}:\mathbf{X}}{\bar{\sigma}}\right) - (g+1)^2 - (g+f)^2 \tag{44}$$

where, in view of approximation $\mathcal{A}_3$, $\mathbb{H}$ is given by

$$\mathbb{H} \equiv \mathbb{p} + \eta(\mathbf{X}\otimes\mathbf{Q} + \mathbf{Q}\otimes\mathbf{X}) \tag{45}$$

$\mathbf{Q}$ by (34), $\mathbf{X}$ by (42) and the criterion parameters κ, α_2, g, C and η are provided in Appendix C. Recall the definitions of the anisotropy tensors $\mathbb{p}$ and $\hat{\mathbb{p}}$ from (15).

In the special case of an isotropic Von Mises matrix ($\mathbb{h} = \hat{\mathbb{h}} = \mathbb{I}$) equation (44) reduces to the form proposed by Gologanu et al. (1997). However, Gologanu et al. had proposed the above form as a heuristic generalization of an axisymmetric criterion derived using a similar limit analysis. In the case of spherical voids in a Hill matrix, from (C.3) one obtains $\lim_{w\to 1} \alpha_2 = 1/3$ and from (C.4) $C = 1$ and $\eta = 0$. Also, (C.2) reduces to

$$\kappa^{\mathrm{BB}} = \frac{3}{2}\sqrt{\frac{5}{(\hat{h}_q + 2\hat{h}_a + 2\hat{h}_t)}} = \frac{3}{2}\left[\frac{2}{5}\frac{h_{\mathrm{L}} + h_{\mathrm{T}} + h_{\mathrm{S}}}{h_{\mathrm{L}}h_{\mathrm{T}} + h_{\mathrm{T}}h_{\mathrm{S}} + h_{\mathrm{S}}h_{\mathrm{L}}} + \frac{1}{5}\left(\frac{1}{h_{\mathrm{TS}}} + \frac{1}{h_{\mathrm{SL}}} + \frac{1}{h_{\mathrm{LT}}}\right)\right]^{-\frac{1}{2}} \tag{46}$$

in terms of Hill's coefficients from Section 4.2 and the upper-bound yield criterion of Benzerga and Besson (2001) is recovered. Note that κ^{BB} is an invariant of tensor $\mathbb{h}$ but $\hat{h}$, $\hat{h}_a$ and $\hat{h}_t$ are only transversely isotropic invariants. In particular, the Gurson yield function is obtained in the limit of spherical voids in an isotropic matrix since $\mathbb{h} = \mathbb{I}$ implies $\kappa^{\mathrm{BB}} = 3/2$.

In the limit of cylindrical voids in a Hill matrix with $\underline{e}_{\mathrm{S}} = \underline{e}_3$, we have $\lim_{w\to\infty} \alpha_2 = 1/2$ $C = 1$, $\eta = 0$ and (C.2) reduces to

$$\kappa^{\mathrm{cyl}} = \sqrt{\frac{3}{\hat{h}_t}} = \sqrt{3}\left[\frac{1}{4}\frac{h_{\mathrm{L}} + h_{\mathrm{T}} + 4h_{\mathrm{S}}}{h_{\mathrm{L}}h_{\mathrm{T}} + h_{\mathrm{T}}h_{\mathrm{S}} + h_{\mathrm{S}}h_{\mathrm{L}}} + \frac{1}{2h_{\mathrm{LT}}}\right]^{-\frac{1}{2}} \tag{47}$$

which is the result obtained by Benzerga and Besson (2001)[2]. In particular, the Gurson yield function for cylindrical cavities in a Von Mises matrix is recovered with $\kappa^{\mathrm{cyl}} = \sqrt{3}$ in that case.

6 Example Yield Loci

The yield surface defined by equation (44) may be visualized as the boundary of a convex region in the Haigh–Westergaard stress space (three-dimensional space with the principal stresses $\Sigma_{\mathrm{I}}, \Sigma_{\mathrm{II}}, \Sigma_{\mathrm{III}}$ as the Cartesian coordinates). It is conventional in plasticity theory to use cylindrical coordinates $z = \Sigma_{\mathrm{m}}$, $r = \sqrt{\boldsymbol{\Sigma}' : \boldsymbol{\Sigma}'} = \sqrt{2/3}\Sigma_e$ and θ such that $\cos(3\theta) = 27/2\det(\boldsymbol{\Sigma}'/\Sigma_e)$. As in equation (1), Σ_e and Σ_{m} are the Von Mises effective stress and mean normal stress, respectively, and θ is the Lode angle. Cross-sections of the yield surface corresponding to the family of planes $\Sigma_{\mathrm{m}} = \mathrm{cste}$ are called π-planes and the cross sections corresponding to $\theta = \mathrm{cste}$ are called meridional planes. It is emphasized that, the yield function (44) being anisotropic, the shape of the yield surface in principal stress space will vary depending on the relative orientations of the principal axes of loading, the axes of orthotropy of the matrix and the axis of symmetry of the void.

In this section, we present cross-sections of the yield surface corresponding to special cases of loading. The first cross-section corresponds to triaxial loadings sharing a common value of Σ_{m}. This cross-section represents the trace of the yield surface on a π-plane. The second cross-section corresponds to axisymmetric loading about the $\underline{e}_{\mathrm{III}}$ axis, $\boldsymbol{\Sigma} = \Sigma_{\mathrm{m}}\mathbf{I} +$

[2]There are two typographical errors in (Benzerga and Besson, 2001) (i) the exponent 1/2 was dropped in print; and (ii) $\Sigma_{\alpha\alpha}$ should read $\Sigma_{11} + \Sigma_{22}$ after their equation (58).

Label	Loading orientation
L_1	$\underline{e}_{\rm I} = \underline{e}_{\rm L}, \underline{e}_{\rm II} = \underline{e}_{\rm T}, \underline{e}_{\rm III} = \underline{e}_{\rm S}$
L_2	$\underline{e}_{\rm I} = \underline{e}_{\rm L}, \underline{e}_{\rm II} = \underline{e}_{\rm S}, \underline{e}_{\rm III} = -\underline{e}_{\rm T}$
L_3	$\underline{e}_{\rm I} = \underline{e}_{\rm L}, \underline{e}_{\rm II} = \frac{1}{\sqrt{2}}(\underline{e}_{\rm T} + \underline{e}_{\rm S}), \underline{e}_{\rm III} = \frac{1}{\sqrt{2}}(-\underline{e}_{\rm T} + \underline{e}_{\rm S})$

Table 2: Orientations of the principal axes of loading relative to the microstructure, corresponding to the yield loci of Figs. 8–11.

$\Sigma^{'}/3(-\underline{e}_{\rm I}\otimes\underline{e}_{\rm I}-\underline{e}_{\rm II}\otimes\underline{e}_{\rm II}+2\underline{e}_{\rm III}\otimes\underline{e}_{\rm III})$. The third cross-section corresponds to in-plane shear loading with a superposed hydrostatic stress, $\mathbf{\Sigma} = \Sigma_{\rm m}\mathbf{I} + \Sigma^{'}/\sqrt{3}(\underline{e}_{\rm I}\otimes\underline{e}_{\rm I} - \underline{e}_{\rm II}\otimes\underline{e}_{\rm II})$. Note that for the latter types of loading, the Von Mises effective stress $\Sigma_e = |\Sigma^{'}|$. Assuming that the Lode angle θ is measured with respect to the $\Sigma^{'}_{\rm III}$ axis in the π-plane, the above two cross-sections correspond to the traces of the yield surface on meridional planes defined by $\theta = n\pi$ and $\theta = (n+1/2)\pi$, respectively, with $n = 0, 1$. In all cases, the values of the stresses are normalized by a reference stress, $\bar{\sigma} \equiv \sigma_{\rm S}$, which is identified with the yield stress of the matrix material along direction of orthotropy $\underline{e}_{\rm S}$. Also, all examples below are shown for a porosity $f = 0.1$.

Four orthotropic materials are considered for the matrix. Their Hill coefficients are listed in Table 1 (see Section 2). We consider two configurations of the microstructure, characterized by the orientation of the void axis relative to the axes of orthotropy of the matrix. In the first case, referred to as the "aligned" configuration, the void axis $\underline{e}_3$ is taken to be aligned with the $\underline{e}_{\rm S}$ axis of orthotropy. In the second case, referred to as the "misaligned" configuration, an arbitrary orientation is chosen for the void axis relative to the matrix, $\underline{e}_3 = 1/7(2\underline{e}_{\rm L} + 3\underline{e}_{\rm T} + 6\underline{e}_{\rm S})$. In the case of the aligned configuration, the effective medium will be orthotropic with the same triad of orthotropy as the matrix material $(\underline{e}_{\rm L}, \underline{e}_{\rm T}, \underline{e}_{\rm S})$. In particular, when the matrix material is transversely isotropic about the $\underline{e}_{\rm S}$ axis (materials 1 and 2 from Table 1), the effective medium will exhibit transverse isotropy about the $\underline{e}_{\rm S}$ axis. On the other hand, the misaligned configuration does not admit any orthotropic symmetry. Three loading cases are considered depending on the orientation of the principal axes of loading $(\underline{e}_{\rm I}, \underline{e}_{\rm II}, \underline{e}_{\rm III})$ relative to the material axes, Table 2. In cases L_1 and L_2, the principal axes of loading are aligned with the axes of orthotropy of the matrix, whereas L_3 corresponds to off-axis loading.

We first start with the case of materials containing spherical voids embedded in anisotropic matrices. In that case, the new criterion reduces to that of Benzerga and Besson (2001). The yield loci corresponding to all four materials from Table 1 are compared in Fig. 8 for various loading configurations. For loadings aligned with the matrix (L_1), Figs. 8(a) and (b) show the traces of the yield surfaces on the π-plane $\Sigma_{\rm m} = 0$ and the yield loci for axisymmetric loading about the $\underline{e}_{\rm III}$ axis, respectively. The yield loci in the π-plane for the isotropic matrix and materials 1–2 are perfect circles. This is a consequence of Hill coefficients h_1, h_2 and h_3 being equal in these materials. By way of contrast, the yield locus of Material 3 is an ellipse. In general, the elliptical shape of the yield locus on the π-plane is a signature of the Hill criterion assumed for the matrix and introduces a Lode angle dependence for the effective yield criterion. For reference, the yield loci of the sound matrices (i.e. for $f = 0$) are cylinders whose cross-sections are similar to the cross-sections in the π plane (shown in parts (a) of Fig. 8 and subsequent figures), but are bigger by a factor $1/(1-f)$.

Since the yield function is indifferent to the sign of stress, the yield surface is symmetric

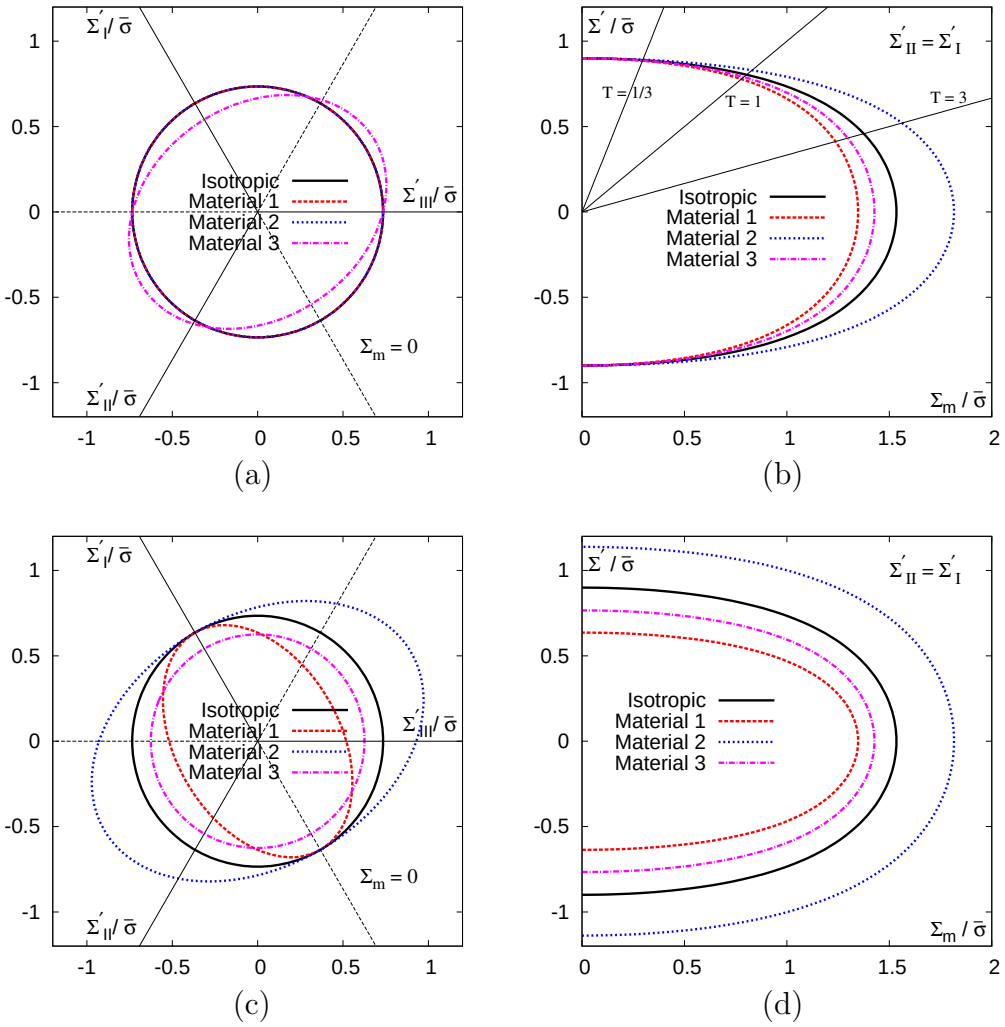

Figure 8: Cross-sections of the yield surface for a spherical cavity with $f = 0.1$ and the four different anisotropic materials from Table 1. The loading orientations L_1–L_3 correspond to Table 2. Orientation L_1 – (a) π-plane with $\Sigma_m = 0$ (b) axisymmetric loading with $\Sigma'_{II} = \Sigma'_I$. Orientation L_3 – (c) π-plane with $\Sigma_m = 0$ (d) axisymmetric loading with $\Sigma'_{II} = \Sigma'_I$. Stresses are normalized by the yield stress of the matrix material under uniaxial tension in the $\underline{e}_S$ direction of orthotropy.

with respect to inversion about the origin (point symmetry). Hence only the halves of the axisymmetric yield loci corresponding to $\Sigma_{\rm m} > 0$ are shown in Fig. 8b. For the spherical voids considered here, the axisymmetric yield loci are also symmetric with respect to the $\Sigma_{\rm m}$ axis. The radial lines in Fig. 8(b) correspond to proportional loading paths, i.e., with fixed stress triaxiality ratio T. In practice, values of T greater than 4 are rarely attained. Notice that even though the yield points themselves may be close to each other, the normals to the yield loci vary considerably from one material to another, especially towards higher values of T.

Figs. 8(c)-(d) show the corresponding yield loci for the off-axis loading case $\rm L_3$. Here, all the yield traces in the π-plane are ellipses centered at the origin. The apparent Lode-angle dependence is thus exacerbated under off-axes loadings. Interestingly, in Fig. 8(c), one may notice that the yield locus for Material 3 is nearly circular in shape, indicating that the Lode angle dependence of the yield criterion may disappear depending on the orientation of loading relative to the material.

Next, consider the case of materials containing oblate voids with $w = 1/5$ in an isotropic matrix, Fig. 9. In this case, the new yield criterion coincides with that of Gologanu et al. (1997). Results for all loading orientations $\rm L_1$–$\rm L_3$ are shown superposed on each other. Figs. 9(a)-(b) show the π-plane cross-sections corresponding to $\Sigma_{\rm m} = 0$ and $\Sigma_{\rm m} = 0.9\Sigma^h$, respectively, where Σ^h designates the yield stress of the effective medium under pure hydrostatic loading. Although barely visible in Fig. 9(a), the non-spherical void shape leads to a slightly oval shape for the yield locus in the π-plane. However, the main effect of void shape is apparent for non-zero values of the mean stress as in Fig. 9(b). Depending on the loading orientation, the centroid of the yield locus moves away from the $\Sigma_{\rm m} = 0$ axis. This effect is also manifest in Figs. 9(c)-(d), which correspond to the cases of axisymmetric and transverse shear loadings, respectively, with a superposed hydrostatic stress. Note that, unlike in the case of spherical voids, these loci do not exhibit symmetry with respect to either coordinate axis.

Consider now the case of oblate voids (again with $w = 1/5$) embedded in an orthotropic matrix (Material 3) in an aligned configuration, i.e., $\underline{e}_3 = \underline{e}_{\rm S}$. The results summarized in Fig. 10 are the counterpart of the results in Fig. 9 when the isotropic matrix is replaced by Material 3. Notice that these yield loci inherit some of the characteristic features from both Figs. 8 and 9. The shape of the yield locus in the π-plane is primarily determined by the anisotropy of the matrix while the location of the centroid is primarily determined by the void shape. However, it is worth noting that the combined effect is not a simple superposition of a shape change due to material texture and a translation due to void shape. This is best seen from the fact that, unlike in Figs. 8(a) and (c), the π-plane yield loci are not ellipses, but assume a general oval shape. Also, the anisotropy of the matrix has a secondary influence on the location of the centroid. Similar results for prolate cavities (not shown) exhibit all the above characteristics, albeit to a lesser extent. The main difference between prolate and oblate cavities is that, all other conditions being the same, oblate cavities exhibit a greater sensitivity to the mean stress (i.e. lower yield stresses at larger values of $\Sigma_{\rm m}$).

Finally, Fig. 11 shows the yield loci for the most general case of oblate cavities ($w = 1/5$) dispersed in an orthotropic matrix (Material 3) in a misaligned configuration ($\underline{e}_3 = 1/7(2\underline{e}_{\rm L} + 3\underline{e}_{\rm T} + 6\underline{e}_{\rm S})$). These results differ from those of Fig. 10 by the orientation chosen for the void axis $\underline{e}_3$. The π-plane yield loci in Figs. 11(a)-(b) reveal general oval shaped cross sections. Comparing Figs. 10(c)-(d) with Figs. 11(c)-(d) shows

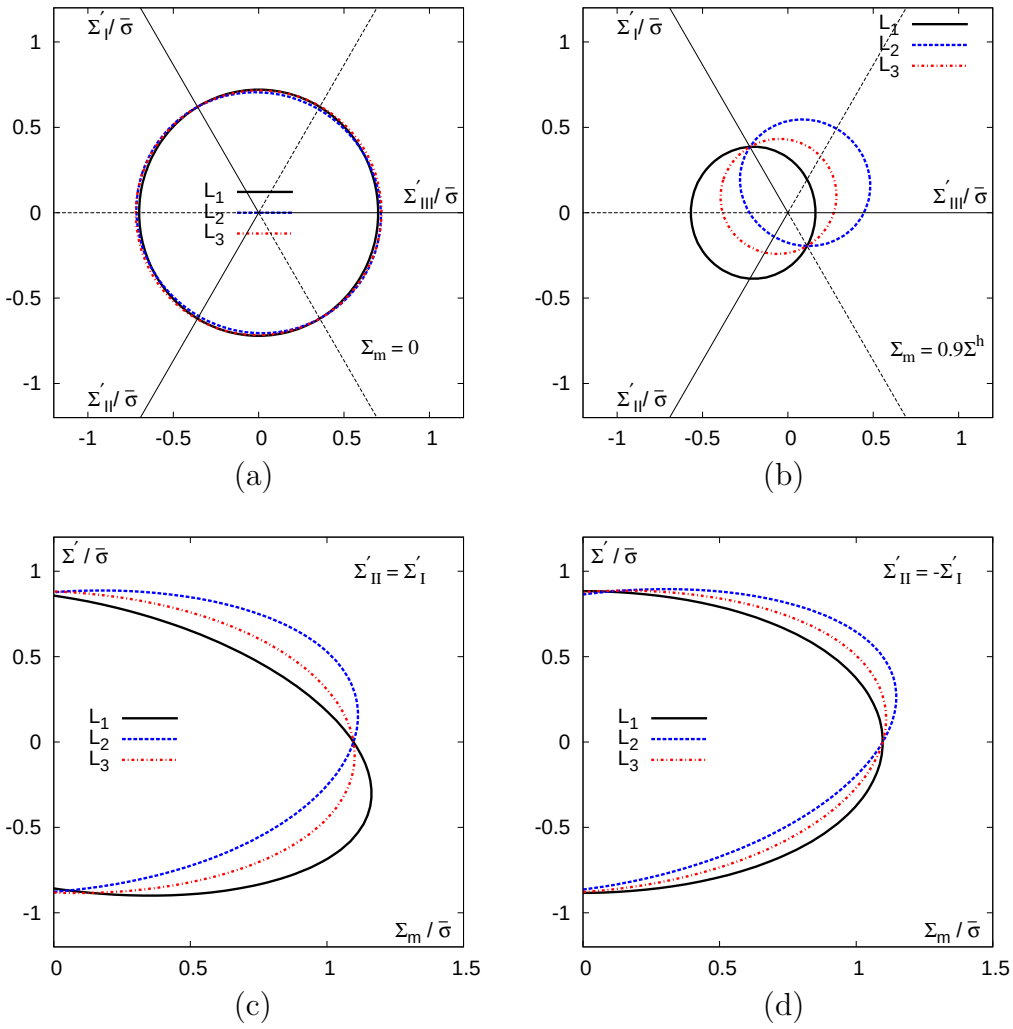

Figure 9: Cross-sections of the yield surface for an oblate cavity with $f = 0.1$, $w = 1/5$ and an isotropic matrix. The loading orientations L_1–L_3 correspond to Table 2. (a) π-plane with $\Sigma_m = 0$ (b) π-plane with $\Sigma_m = 0.9\Sigma^h$ (c) axisymmetric loading with $\Sigma'_{II} = \Sigma'_I$ (d) in-plane shear with superposed hydrostatic stress, $\Sigma'_{II} = -\Sigma'_I$. Stresses are normalized by the yield stress of the matrix material under uniaxial tension in the $\underline{e}_S$ direction of orthotropy.

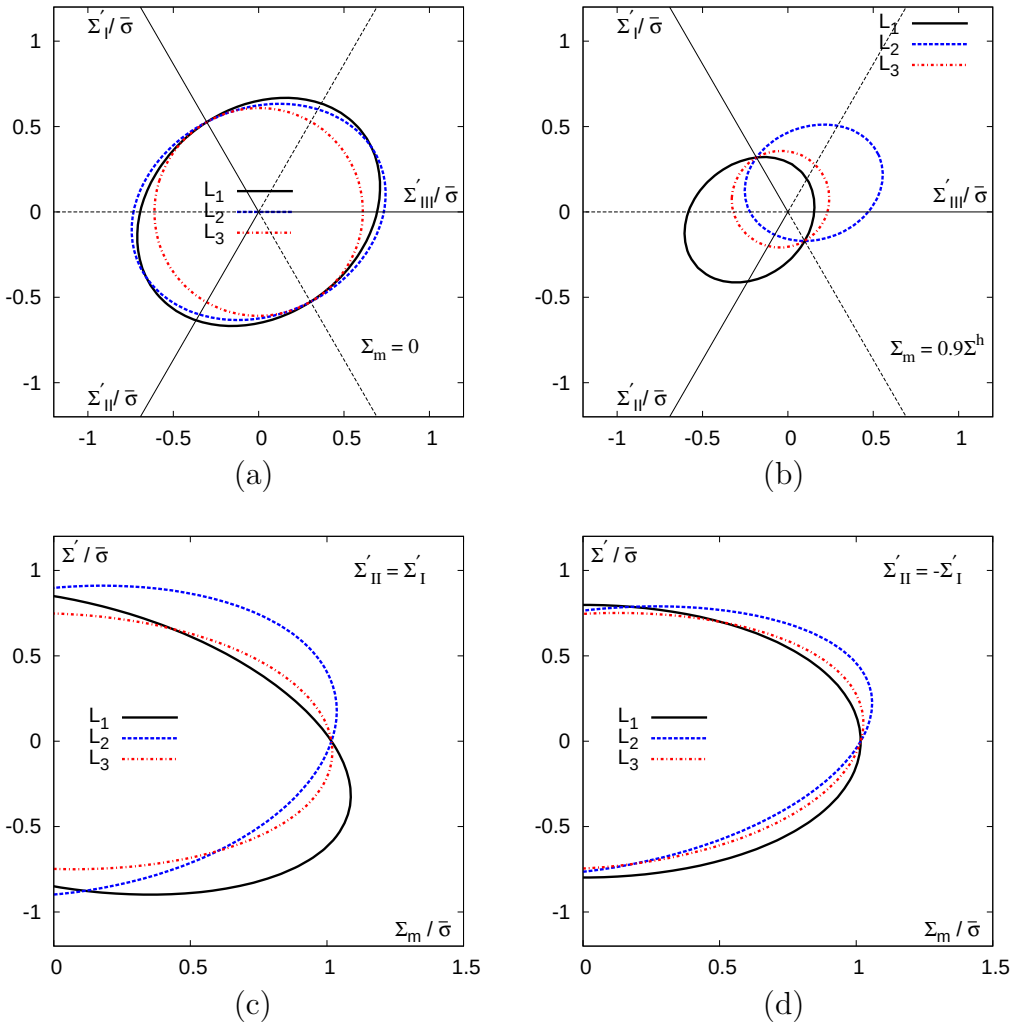

Figure 10: Cross-sections of the yield surface for an oblate cavity with $f = 0.1$, $w = 1/5$ and Material 3 from Table 1. Aligned microstructure with the void axis $\underline{e}_3 = \underline{e}_S$. The loading orientations L_1–L_3 correspond to Table 2. (a) π-plane with $\Sigma_m = 0$ (b) π-plane with $\Sigma_m = 0.9\Sigma^h$ (c) axisymmetric loading with $\Sigma'_{II} = \Sigma'_I$ (d) in-plane shear with superposed hydrostatic stress, $\Sigma'_{II} = -\Sigma'_I$. Stresses are normalized by the yield stress of the matrix material under uniaxial tension in the $\underline{e}_S$ direction of orthotropy.

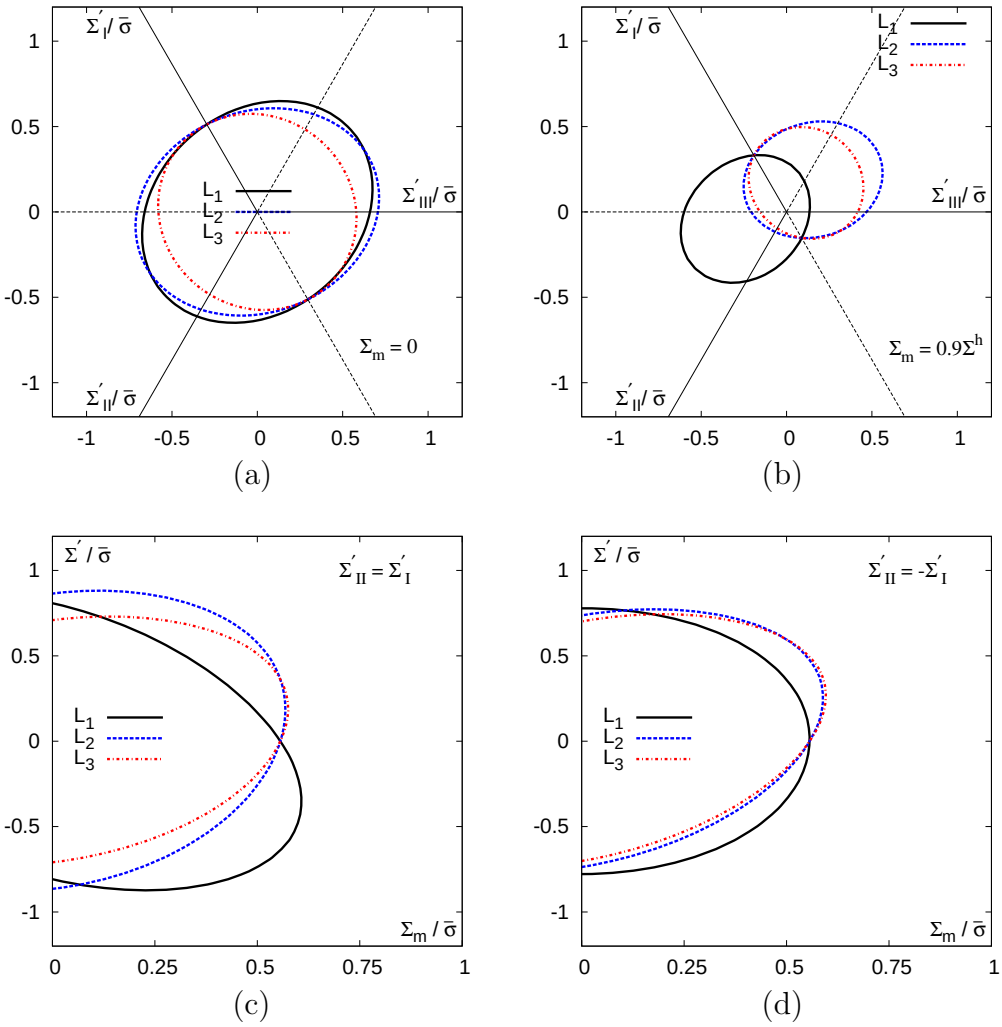

Figure 11: Cross-sections of the yield surface for an oblate cavity with $f = 0.1$, $w = 1/5$ and Material 3 from Table 1. Misaligned microstructure with the void axis $\underline{e}_3 = 1/7(2\underline{e}_\mathrm{L} + 3\underline{e}_\mathrm{T} + 6\underline{e}_\mathrm{S})$. The loading orientations L_1–L_3 correspond to Table 2. (a) π-plane with $\Sigma_\mathrm{m} = 0$ (b) π-plane with $\Sigma_\mathrm{m} = 0.9\Sigma^h$ (c) axisymmetric loading with $\Sigma'_\mathrm{II} = \Sigma'_\mathrm{I}$ (d) in-plane shear with superposed hydrostatic stress, $\Sigma'_\mathrm{II} = -\Sigma'_\mathrm{I}$. Stresses are normalized by the yield stress of the matrix material under uniaxial tension in the $\underline{e}_\mathrm{S}$ direction of orthotropy.

that there is a drastic reduction in the yield stresses at higher triaxialities in the case of the misaligned microstructure, indicating that the evolution of the microstructure due to sustained deformation can lead to significant weakening of the material.

While the analytical yield criterion, equation (44), has been derived using a rigorous variational approach, due to the approximations introduced in the derivations it is unclear whether the final result respects the upper-bound character of the approach. We have developed a numerical method to derive rigorous upper-bound yield loci for anisotropic materials containing spheroidal voids and subjected to axisymmetric loading about the void axis. The method is based on limit-analysis using a large number of velocity fields from the Lee-Mear decomposition (Lee and Mear, 1992), and has the property that it yields nearly exact results for the yield criterion in the particular case when the material exhibits transverse isotropy about the void axis. A more detailed study aimed at validation of the analytical criterion by comparison to the numerical upper-bound yield loci will be published in a forthcoming paper.

7 Microstructure Evolution

To close the constitutive formulation, evolution equations are needed for the microstructural variables that enter the criterion, i.e., void volume fraction, aspect ratio and orientation. Once these are specified, the constitutive equations can be integrated using a suitable scheme to obtain the stress-strain response of the material for specified loading paths.

7.1 Evolution of Porosity

The evolution of void volume fraction, or porosity, follows directly from the assumption of an incompressible matrix so that

$$\frac{\dot{f}}{1-f} = D_{kk} \tag{48}$$

where $\mathbf{D}$ is entirely due to plastic deformation since elasticity is neglected. Given that the matrix obeys the normality flow rule, so does the effective material (Hill, 1967; Gurson, 1977):

$$D_{ij} = \Lambda \frac{\partial \mathcal{F}}{\partial \Sigma_{ij}}(\mathbf{\Sigma}) \tag{49}$$

where $\mathcal{F}(\mathbf{\Sigma})$ denotes the yield function (44) and Λ the plastic multiplier. Combining (48) and the hydrostatic part of (49) we obtain the evolution equation for the porosity

$$\dot{f} = (1-f)\Lambda \frac{\partial \mathcal{F}}{\partial \Sigma_{\mathrm{m}}} \tag{50}$$

Thus, the evolution of porosity follows directly from the yield criterion. With the results of Figs 8-11 in mind, the following is worth noting. While the loci appear to be close to each other in the practical range of stress triaxialities the *normal* to the loci can vary considerably, even at low T. This has important implications for the evolution of the microstructure, as the evolution laws for the porosity and void shape are formulated in

terms of the macroscopic plastic rate of deformation, which is normal to the yield locus. Hence, small differences in the yield loci can lead to large differences in the evolution of microstructural variables.

7.2 Evolution of Void Shape

7.2.1 Basic form

Since the trial velocity field (17) contains a non-axisymmetric component, the model can be used to deliver evolution laws of two independent aspect ratios[3]. However, consistent with approximation $\mathcal{A}_1$, the void aspect ratio w is taken to represent the effective shape of the three-dimensional void, interpreting b_1 as the transverse semi-axis of an 'equivalent spheroid' whose volume equals that of the ellipsoid. For convenience, we define a void shape parameter $S \equiv \ln w$, so that $S > 0$ for prolate voids and $S < 0$ for oblate voids, Fig. 7. Thus,

$$\dot{S} = \frac{\dot{w}}{w} = \frac{\dot{a}_1}{a_1} - \frac{\dot{b}_1}{b_1} \tag{51}$$

To evaluate the right-hand side term in (51), we assume that the void is deforming homogeneously with rate of deformation $\mathbf{D}^v$, naturally defined by

$$D^v_{ij} = \langle d_{ij} \rangle_\omega = \frac{1}{2\omega} \int_{\partial\omega} (v_i n_j + v_j n_i) dS \tag{52}$$

where $\underline{n}$ is the unit normal to the boundary of the void. With the above interpretation in mind, it follows from (51) that

$$\dot{S} = D^v_{33} - \frac{1}{2}(D^v_{11} + D^v_{22}) \tag{53}$$

with the components of $\mathbf{D}^v$ calculated based on (52) and the chosen microscopic velocity fields in (17). Eliminating A and $\boldsymbol{\beta}$ using equations (B.3), we obtain

$$\mathbf{D}^v = \mathbf{D} + 3\left(\frac{1}{f}\mathbf{X}^v - \mathbf{X}\right) D_{\mathrm{m}} \tag{54}$$

where tensor $\mathbf{X}^v$ is defined similar to $\mathbf{X}$ in (42) with α_2 replaced by α_1. Combining (53) and (54) one gets

$$\dot{S} = \frac{3}{2} D'_{33} + 3\left[\frac{1 - 3\alpha_1}{f} + 3\alpha_2 - 1\right] D_{\mathrm{m}} \tag{55}$$

This equation constitutes the basic form for the evolution of void shape and does include an implicit dependence upon matrix anisotropy through the macroscopic rate of deformation, $\mathbf{D}$, which derives from yield criterion (44) by normality.

[3]Note that such laws would be crude, since the assumed velocity fields of Section 5 do not depend on Hill's anisotropy factors. In actuality, the exact velocity field must be affected by the anisotropy.

7.2.2 Alternative Approach

An alternative expression for the average rate of deformation of the void $\mathbf{D}^v$ was derived by Ponte Castañeda and Zaidman (1994) using a micromechanical approach extending the classical Eshelby analysis (Eshelby, 1957) to the case of finite porosities. Their expression reads

$$\mathbf{D}^v = \mathbb{A} : \mathbf{D}, \qquad \mathbb{A} = [\mathbb{I} - (1-f)\mathbb{S}]^{-1} \tag{56}$$

where $\mathbb{A}$ may be termed the strain concentration tensor and $\mathbb{S}$ is the Eshelby tensor for a spheroidal inclusion in an incompressible linear elastic isotropic matrix. One may use (56) in place of (54) in (53) to obtain an alternate estimate for the evolution of the shape parameter. Since a simple closed form expression for $\dot{S}$ of the type (55) can not be found in this case, implementing this approach involves evaluation of the strain concentration tensor $\mathbb{A}$, and hence $\mathbf{D}^v$, based on the current values of f and S and using (53) to evaluate $\dot{S}$. In this stiffness-based approach, the derived expression for $\mathbf{D}^v$ is independent of the microscopic velocity fields.

It must be emphasized, however, that neither the basic nor the alternate expression for $\mathbf{D}^v$ capture the complex effect of stress triaxiality that leads to cavity flattening under a major axial stress evidenced in finite element simulations (Budiansky et al., 1982; Koplik and Needleman, 1988). In addition, similar FE calculations have revealed an effect of porosity on the magnitude of the deviatoric term in (55). This effect is implicitly contained in the alternate form (56), but the dependence is weaker than in FE calculations. Therefore, at present it does not seem to be possible to avoid completely all heuristics in the evolution law of void shape. In a companion paper, we analyze possible heuristic extensions of (55). Here, it suffices to investigate the capability of this evolution law at capturing the nontrivial coupling between void growth and plastic anisotropy.

7.3 Evolution of Void Orientation

Under general loading conditions, the orientation of the void axis $\underline{e}_3$ evolves as a result of the macroscopic spin of the material in addition to the local plastic distortion. While the simplest proposal would be to assume that the spin rate of the voids is equal to the continuum spin, micrographic evidence of evolving material texture in notched tensile specimens (Benzerga, 2000) suggests that this is not necessarily the case (see Figure 12).

Based on a non-linear homogenization analysis, Kailasam and Ponte Castaneda (1998) have developed an expression for the void spin rate, which reads

$$\mathbf{\Omega}^v = \mathbf{\Omega} - \mathbb{C} : \mathbf{D} \tag{57}$$

where $\mathbf{\Omega}^v$ and $\mathbf{\Omega}$ represent the void and continuum spin tensors respectively. $\mathbb{C}$ represents the fourth order spin concentration tensor, which is given by

$$\mathbb{C} = -(1-f)\mathit{\Pi} : \mathbb{A} \tag{58}$$

where $\mathit{\Pi}$ is the Eshelby rotation tensor for a spheroidal inclusion in an incompressible linear matrix (Eshelby, 1957). Simplified expressions for $\mathbb{S}$ and $\mathit{\Pi}$ for the cases of prolate and oblate spheroidal inclusions are provided in (Eshelby, 1957). The evolution of the void orientation may then be obtained using the kinematical relationship

$$\dot{\underline{e}}_3 = \boldsymbol{\omega} \cdot \underline{e}_3, \qquad \boldsymbol{\omega} = \mathbf{\Omega}^v + \mathbf{\Omega}^l \tag{59}$$

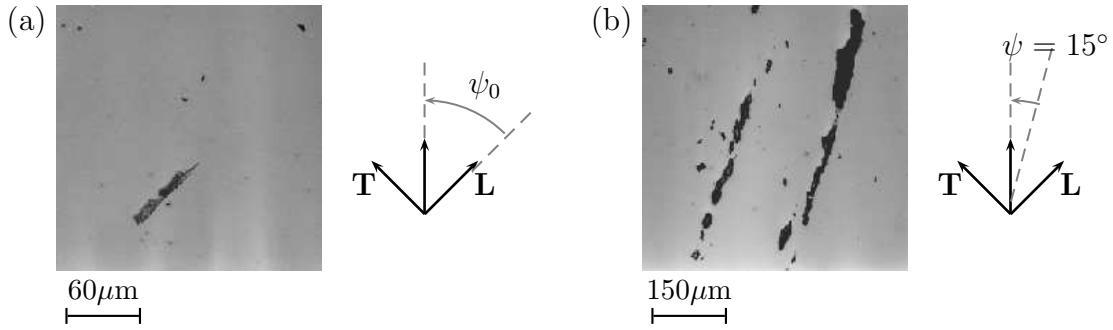

Figure 12: Void rotation under off-axes triaxial loading of steel. (a) Initial configuration: elongated sulfide inclusion oriented at $\psi_0 = 45^\circ$ from the vertical loading direction. (b) Deformed configuration: elongated cavities located in the neck of a notched bar and oriented at $\psi \approx 15^\circ$ from the vertical loading direction.

where $\mathbf{\Omega}^l$ is an antisymmetric tensor given by

$$\Omega^l_{12} = 0, \quad \Omega^l_{i3} = \frac{w^2+1}{w^2-1} D^v_{i3} \qquad (i = 1, 2, \quad w \neq 1) \tag{60}$$

in the coordinate frame associated with the void (see Kailasam and Ponte Castaneda, 1998).

It may be remarked that the actual derivation of (57) assumes that the matrix is isotropic, and hence is strictly not applicable to the case of an anisotropic matrix like Hill's. Nevertheless, one can see that, as in equation (55) for the void shape evolution, equation (57) includes an implicit dependence of $\mathbf{\Omega}^v$ on material anisotropy through the macroscopic rate of deformation, $\mathbf{D}$. Hence, in the practical range of material anisotropy parameters, we may consider equation (57) as the best available estimate of the void spin rate.

7.4 Example

In this section, we compare the predictions of the analytical model, consisting of the yield function (44), flow rule (49) and the microstructure evolution laws (50) and (55), with the finite-element results presented in Section 2 for axisymmetric proportional loading at a moderate stress triaxiality ratio of $T = 1$. Since the materials considered are transversely isotropic, the void orientation does not change during loading ($\boldsymbol{\omega} \equiv \mathbf{0}$). For comparison, responses obtained using the alternative law for void shape evolution, i.e., equations (53) and (56), are also investigated. The constitutive equations are integrated using a backward Euler scheme. Strain hardening in the matrix is incorporated using the energy balance approach of Gurson (1977), whereby the cumulative plastic strain $\bar{\epsilon}$ is evolved through

$$\mathbf{\Sigma} : \mathbf{D} = (1 - f)\bar{\sigma}\dot{\bar{\epsilon}} \tag{61}$$

The current yield stress in the matrix $\bar{\sigma}$ is determined using the same power law hardening model used in the FE calculations as described in Section 2. Elasticity is included in the analytical model results using a hypoelastic form for the elastic constitutive law and assuming additive decomposition of the deformation rate tensor into elastic and plastic parts.

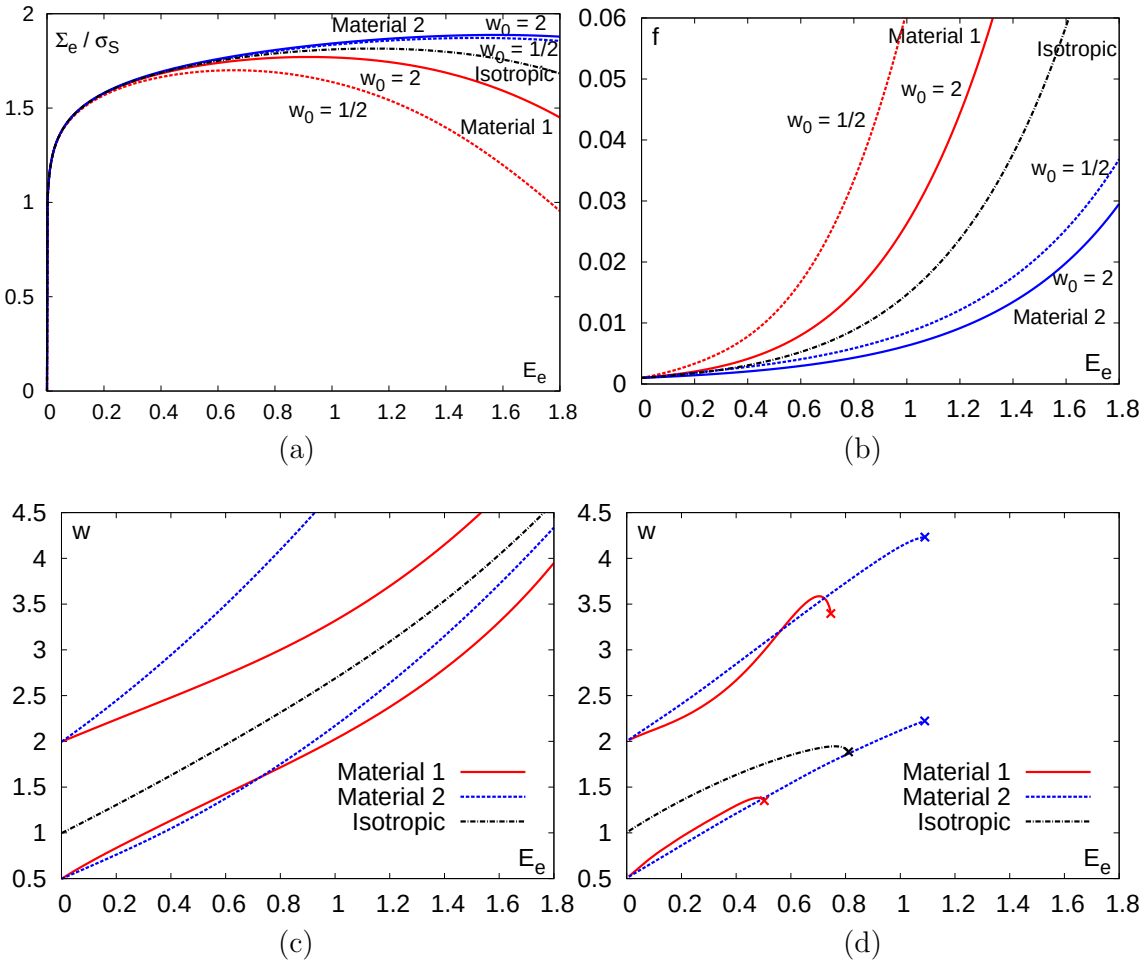

Figure 13: Model predictions for the effective material response under axisymmetric loading, corresponding to the unit-cell results of Fig. 5, Section 2: (a) Stress-strain response (b) Evolution of porosity (c) Evolution of void aspect ratio. The unit-cell results for the evolution of the void aspect ratio (not shown in Fig. 5) are shown in (d).

Figs. 13(a) and (b) show the stress versus strain and porosity versus strain curves predicted by the model. These results correspond to the unit-cell results of Figs. 5(a) and (b), respectively. Recall that the unit-cell results had evidenced a non-trivial coupling between the effects of void shape and plastic anisotropy of the matrix, the effect of void shape on the porosity rate being enhanced in the case of Material 1 and barely detectable in the case of Material 2. Comparison with the model predictions in Fig. 13(a)-(b) shows that the qualitative features of the unit-cell results are very well reproduced by the model. In addition, the evolution of the void aspect ratio depicted in Fig. 13(c) shows that the model predictions yield a reasonably good match with the unit-cell results, which are summarized in Fig. 13(d). In the latter figure, the symbol (x) indicates the onset of void coalescence, which is not accounted for by the analytical model.

It is worth emphasizing that such qualitative behavior, notably the weak effect of void shape on void growth for material 2, is predicted without any heuristics in the evolution law (55). For better quantitative predictions, however, a heuristic "void interaction" parameter q could be introduced in the spirit of Gologanu et al. (1997). Further discussion of these issues may be found in a forthcoming companion paper. For comparison pur-

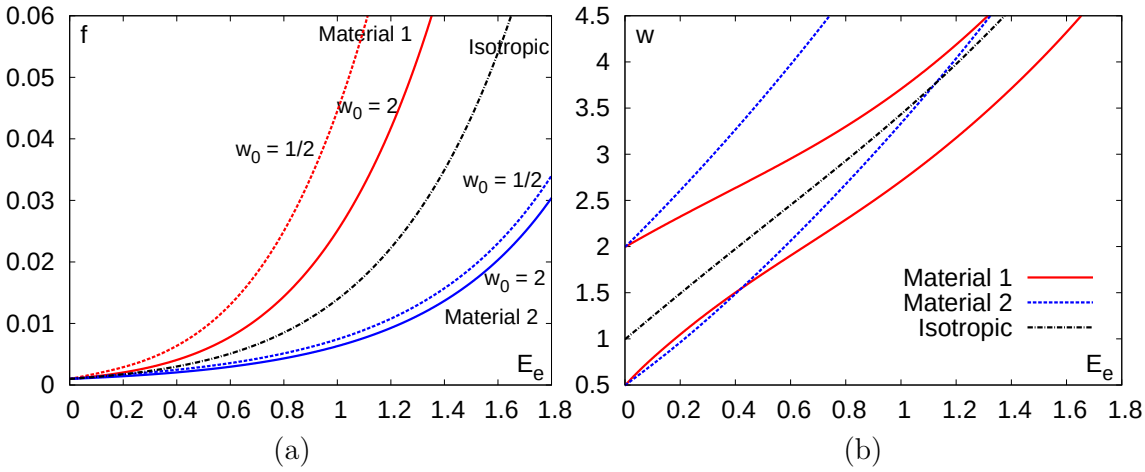

Figure 14: Model predictions for the porosity f and void aspect ratio w using the alternate form (56) for void shape evolution in (53). Compare with Fig. 13(b) and (c).

poses, Fig. 14 shows the evolutions of porosity f and void aspect ratio w as predicted by the alternate evolution law for w due to Ponte Castañeda and Zaidman (1994) (see Section 7.2.2). Just like the proposed model, the alternate model does a good a job at predicting the qualitative trends at $T = 1$ for both materials.

8 Conclusion and Outlook

Using nonlinear homogenization theory, limit analysis and elements from Eshelby micromechanics, a new model has been developed for plastically deforming solids containing spheroidal voids. Motivated by the experimental evidence of fracture and toughness anisotropy in a class of structural materials and by direct numerical simulations of void growth to coalescence, emphasis was laid on coupled effects of matrix material anisotropy and void shape. Notable among the model features are the following:

- A closed form expression for the effective yield locus was obtained which is applicable to arbitrary loadings, i.e, not necessarily aligned with the microstructure, and arbitrary microstructures, i.e., principal directions of orthotropy not necessarily tied to the voids.

- The model has the capability to predict a much broader range of damage and fracture behaviors than with currently available models. For example, it picks up an apparent Lode-angle dependence as well as a shift of the yield surface in the π-plane for non vanishing amounts of hydrostatic stress.

- In the case of transversely isotropic materials and axisymmetric loadings, the model delivers quasi-exact results with any errors being associated with the cutoff in the velocity fields. It is demonstrated that the new yield criterion reduces to previously established results in the literature for the special cases of spheroidal voids in an isotropic matrix and spherical voids in a Hill matrix. The Gurson model is a special limit case of the model.

- Comparison with results of unit cell calculations using the finite element method has demonstrated the potential capabilities of the model at predicting complex microstructure evolution.

In addition, some of the model characteristics and limitations are common to other porous plasticity models, namely:

- Most attributes of the anisotropic plasticity model assumed at the microscale do not translate to the macroscale. In particular, the macroscopic behavior is not ideally plastic, it is sensitive to pressure and leads to dilation. In addition, macroscopic anisotropy evolves with deformation and carries the signature of the microstructure.

- Among the things that the model does not deliver for arbitrary loadings or general matrix anisotropies are the exact *microscopic* velocity fields. From the outset, this has not been the objective. The model delivers approximate but accurate *macroscopic* yield criteria.

- The closed form expression of the yield criterion was obtained using approximations that do not necessarily preserve the upper-bound character. For that reason, we have devoted a thorough numerical study to assess the approximations made. Complete validation of the new model would also require a critical assessment of microstructure evolution laws beyond the preliminary comparisons offered in Fig. 13. This requires extensive finite element analyses of anisotropic porous unit cells under controlled loading conditions. Corresponding numerical methods and results are the subject of a forthcoming companion paper.

Acknowledgments

The authors acknowledge partial support from the National Science Foundation under Grant CMMI-0748187. We are indebted to the anonymous reviewer whose comments led us to discover an error in an earlier version of Appendix B.

Appendix A. Rationale for Approximation $\mathcal{A}_2$

The microscopic deformation resulting from the trial expansion field $\underline{v}^A$ fluctuates within the RVE. Simplifying these fluctuations amounts to analyzing the variations of functions $F(u)$ and $G(u)$ introduced in (35). We first examine the limits of these functions, aided by the Maple software. In the limit $u \to 0$ (i.e., spherical void) we get:

$$\lim_{u\to 0} F^2(u) = \lim_{y\to 0} \frac{1}{y^2}\langle d_{\text{eq}}^{A^2}\rangle_{(\beta,\varphi)} = \frac{4}{5}(\hat{h}_q + 2\hat{h}_t + 2\hat{h}_a), \tag{A.1}$$

and

$$\lim_{y\to 0}\langle d_{33}^{A}\rangle_{(\beta,\varphi)} = 0 \tag{A.2}$$

whereas in the limit $y \to \infty$ (i.e., cylindrical void in the prolate case and a "sandwich" in the oblate case) we obtain:

$$\begin{cases} \lim\limits_{u\to\infty} F^2(u) = \lim\limits_{y\to\infty} \dfrac{1}{y^2}\langle d_{\text{eq}}^{A^2}\rangle_{(\beta,\varphi)} & = 3\hat{h}_t & \text{(p)} \\ \lim\limits_{u\to 1} F^2(u) = \lim\limits_{y\to\infty} \langle d_{\text{eq}}^{A^2}\rangle_{(\beta,\varphi)} & = 9\hat{h}_q(3\pi B_{22} + 4B_{21})^2 + 6\hat{h}_a(\pi B_{21} + 12B_{22})^2 & \text{(o)} \end{cases} \tag{A.3}$$

and

$$\begin{cases} \lim\limits_{y\to\infty} \langle d_{33}^{A}\rangle_{(\beta,\varphi)} & = 0 & \text{(p)} \\ \lim\limits_{y\to\infty} \langle d_{33}^{A}\rangle_{(\beta,\varphi)} & = 12B_{21} + 9\pi B_{22} & \text{(o)} \end{cases} \tag{A.4}$$

where B_{21} and B_{22} were introduced in (18), $\hat{h}_q$ is defined by (37) and

$$\hat{h}_t \equiv \frac{\hat{h}_{11} + \hat{h}_{22} + 2\hat{h}_{66} - 2\hat{h}_{12}}{4}, \qquad \hat{h}_a \equiv \frac{\hat{h}_{44} + \hat{h}_{55}}{2}. \tag{A.5}$$

Here, $\hat{h}_{ij}$ are the components of tensor $\hat{\mathbb{h}}$ expressed using Voigt's condensation, with respect to the basis $(\underline{e}_i)$ associated with the voids[4]. The above limits call for some observations: (i) in the prolate case, $\langle d_{\text{eq}}^{A^2}\rangle_{(\beta,\varphi)}$ behaves asymptotically as y^2, hence the change of variable $u(y)$ in (35); (ii) in the oblate case, the asymptotic behavior at ∞ is different, hence the different mapping $u(y)$; and (iii) most importantly, all limits of $F(u)$ are finite. The only singular behavior is in the neighborhood of 0 for function $G(u)$, which is tied to the term $\langle d_{33}^{A}\rangle_{(\beta,\varphi)}$ via (35). This behavior is peculiar to the spherical void when considered in the limit $u \to 0$. Nevertheless, the corresponding term in equation (33) drops out rigorously in the limit of a spherical void due to the property (A.2), which is a consequence of the fact that the expansion velocity field $\underline{v}^{\text{A}}$ reduces to a spherically symmetric field in the limit of a spherical void. Under such circumstances, the yield criterion can be derived without recourse to approximation $\mathcal{A}_2$ but the final expression would be consistent with that obtained in the general case using $\mathcal{A}_2$.

Next, we show that $F(u)$ behaves well in between the above limits. In doing so, we realize that the function to be studied is that for which the minimum overall dissipation is obtained when minimizing over the B_{2m} factors of the velocity field ($m = 0, 1, 2$).

[4]The values of $\hat{h}_t$ and $\hat{h}_a$ are invariant with respect to the choice of axes $\underline{e}_1$ and $\underline{e}_2$ transverse to the symmetry axis of the void.

This function is denoted by $F^{\min}(u)$ for the sake of clarity. Numerically, $F^{\min}(u)$ may be determined for given plastic anisotropy, microstructural parameters f and w and for any loading path. The involved velocity fields do depend upon the plastic anisotropy tensor $\mathbb{h}$ through factors B_{2m}. For illustration, Figs. 15 and 16 (solid lines) show such functions $F^{\min}(u)$ for the isotropic matrix and one anisotropic material, for states of purely hydrostatic loading. Similar results were derived for the other materials listed in Table 1. In the prolate case (Fig. 15) $F^{\min}$ is more conveniently plotted against the eccentricity e as the spatial variable within the RVE. The bounds for e and u in these plots depend on the specific choices made for porosity f and void aspect ratio w. The key point is that, despite their complicated expressions, the functions $F^{\min}(u)$ exhibit smooth variations between their finite limits. This is the rationale for replacing $F(u)$ with $\bar{F}$. The reasoning behind replacing $G(u)$ and $H(u)$ with constants is similar and leads to the proposed simplification of fluctuating deformation fields.

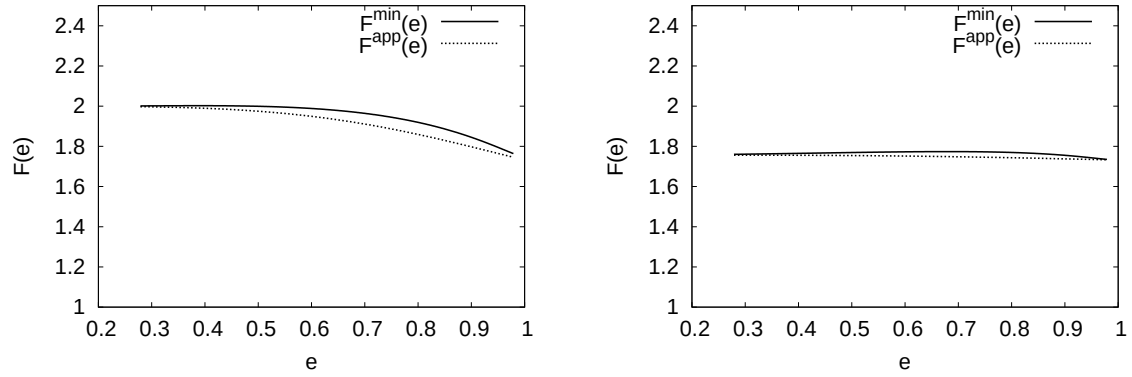

Figure 15: Numerically determined $F^{\min}(e)$ minimizing the overall dissipation under hydrostatic loading, and its approximate closed form $F^{\text{app}}(e)$ in (C.7) for a prolate void with $f = 0.001$ and $w = 5$: (a) Isotropic matrix; (b) Material 1 from Table 1.

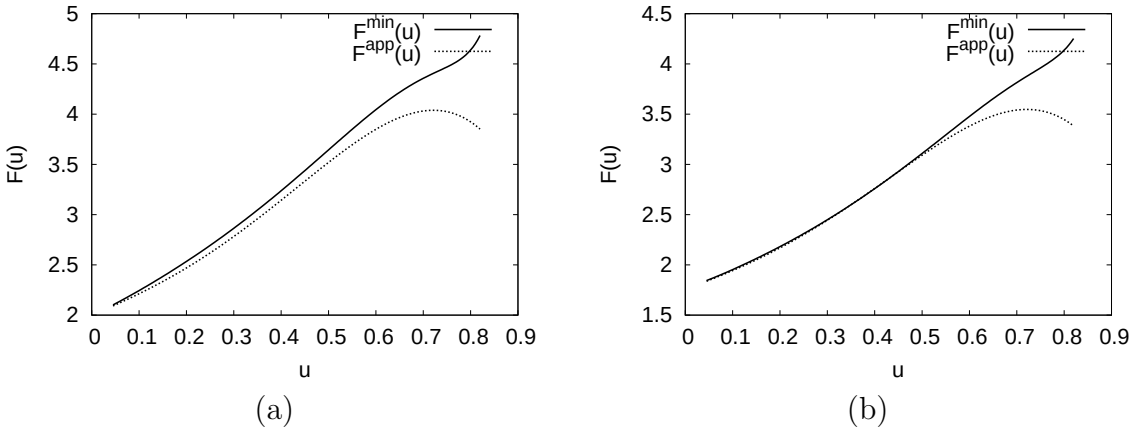

Figure 16: Numerically determined $F^{\min}(u)$ minimizing the overall dissipation under hydrostatic loading, and its approximate closed form $F^{\text{app}}(e)$ in (C.8) for an oblate void with $f = 0.001$ and $w = 1/5$: (a) Isotropic matrix; (b) Material 1 from Table 1.

Appendix B. Derivation of yield criterion (40)

To obtain form (40) of the yield criterion, we first separate mean and deviatoric parts of $\boldsymbol{\Sigma}$ in the parametric equation (5) such that

$$\Sigma_{kk} = 3\frac{\partial \Pi}{\partial D_{kk}}, \qquad \Sigma'_{ij} = \frac{\partial \Pi}{\partial D'_{ij}} \tag{B.1}$$

Writing the axisymmetric tensor $\mathbf{D}^A$ in the form $D^A_{ij} = D^A_{kk} X_{ij}$ with tensor $\mathbf{X}$ given by (42) and using the expressions for the expansion velocity field $\underline{v}^A$ (18)–(19) in the boundary condition (23), one can show that

$$D^A_{kk} = 3y_2, \qquad \alpha_2 \equiv \frac{D^A_{11}}{D^A_{kk}} = \frac{1}{3} - \frac{b_2}{c} F_2(\lambda_2) \tag{B.2}$$

where $F_2(\lambda)$ is defined by (26). Using (42) and (B.2) in (22), D_{kk} and $\mathbf{D}'$ are related to A and $\boldsymbol{\beta}$ through

$$A = \frac{1}{3y_2} D_{kk}, \quad \boldsymbol{\beta} = \mathbf{D}' + \frac{1}{3} D_{kk}(\mathbf{I} - 3\mathbf{X}) \tag{B.3}$$

Using the change of variables $(D_{kk}, \mathbf{D}') \to (A, \boldsymbol{\beta})$ equation (B.1) is rewritten in the form

$$3y_2 \Sigma_{ij} X_{ij} = \frac{\partial \Pi}{\partial A}, \qquad \Sigma'_{ij} = \frac{\partial \Pi}{\partial \beta_{ij}} \tag{B.4}$$

Next, use of the chain rule in conjunction with equation (39) yields

$$\frac{\partial \Pi}{\partial A} = \frac{\bar{F}}{\sqrt{\hat{h}_q}} \frac{\partial \Pi}{\partial \tilde{\mathbf{A}}} : \mathbf{Q}, \quad \frac{\partial \Pi}{\partial \boldsymbol{\beta}} = \sqrt{\hat{h}_q} \bar{G} \frac{\partial \Pi}{\partial \tilde{\mathbf{A}}} + \bar{H} \frac{\partial \Pi}{\partial \tilde{\mathbf{B}}} \tag{B.5}$$

where evaluation of the Jacobian must be carried out with care given that change of variable (39) is not one to one[5]. From expression (38) for the plastic dissipation, one formally gets

$$\frac{\partial \Pi}{\partial \tilde{\mathbf{A}}} = C_1 \frac{2}{3} \hat{\mathbb{p}} : \tilde{\mathbf{A}}, \quad \frac{\partial \Pi}{\partial \tilde{\mathbf{B}}} = C_2 \frac{2}{3} \hat{\mathbb{p}} : \tilde{\mathbf{B}}, \qquad \hat{\mathbb{p}} = \mathbb{J} : \hat{\mathbb{h}} : \mathbb{J}, \tag{B.6}$$

where C_1 and C_2 are positive scalar-valued functions. One can solve for the unknown C_1 by substituting $(\text{B.6})_1$ in $(\text{B.5})_1$. Using the above derived expression for $\partial \Pi / \partial \tilde{\mathbf{A}}$ in (B.5) and upon simplification using (B.4), one obtains

$$\frac{\partial \Pi}{\partial \tilde{\mathbf{A}}} = \frac{(\boldsymbol{\Sigma} : \mathbf{X})}{\sqrt{\hat{h}_q}} \frac{2y_2}{\bar{F}} \hat{\mathbb{p}} : \{\mathbf{Q} + \mathbf{R}\}, \quad \frac{\partial \Pi}{\partial \tilde{\mathbf{B}}} = \frac{1}{\bar{H}} \left[\boldsymbol{\Sigma}' - \frac{2y_2 \bar{G}}{\bar{F}} (\boldsymbol{\Sigma} : \mathbf{X}) \hat{\mathbb{p}} : \{\mathbf{Q} + \mathbf{R}\} \right] \tag{B.7}$$

where the tensor $\mathbf{R}$ is defined by

$$\mathbf{R} \equiv \frac{[(\mathbf{Q} : \hat{\mathbb{p}} : \mathbf{Q})\boldsymbol{\beta}/A - (\mathbf{Q} : \hat{\mathbb{p}} : \boldsymbol{\beta}/A)\mathbf{Q}]}{\left[\frac{3}{2}\bar{F}/\bar{G} + (\mathbf{Q} : \hat{\mathbb{p}} : \boldsymbol{\beta}/A)\right]} \tag{B.8}$$

[5] We keep the notation $\Pi(\tilde{\mathbf{A}}, \tilde{\mathbf{B}})$ for what should be $\tilde{\Pi}(\tilde{\mathbf{A}}, \tilde{\mathbf{B}})$

Notice that $\mathbf{R} \equiv \mathbf{0}$ if $\boldsymbol{\beta} \propto \mathbf{Q}$, i.e. for states of axisymmetric deformation about the void axis. Also note that, since $\boldsymbol{\beta}/A = 3y_2(\mathbf{D}/D_{kk} - \mathbf{X})$ from (B.3) and $y_2 \to 0$ for a spherical void, $\mathbf{R} \equiv \mathbf{0}$ in the limit case of a spherical void.

From the chain rule and the definitions of $\tilde{A}_{\text{eq}}$ and $\tilde{B}_{\text{eq}}$, we get

$$\left(\frac{\partial \Pi}{\partial \tilde{A}_{\text{eq}}}\right)^2 = \frac{3}{2}\frac{\partial \Pi}{\partial \tilde{\mathbf{A}}} : \mathbb{p} : \frac{\partial \Pi}{\partial \tilde{\mathbf{A}}}, \quad \left(\frac{\partial \Pi}{\partial \tilde{B}_{\text{eq}}}\right)^2 = \frac{3}{2}\frac{\partial \Pi}{\partial \tilde{\mathbf{B}}} : \mathbb{p} : \frac{\partial \Pi}{\partial \tilde{\mathbf{B}}}, \quad \mathbb{p} = \mathbb{J} : \mathbb{h} : \mathbb{J} \tag{B.9}$$

Finally, evaluation of the integral in (38) and elimination of the ratio $\tilde{A}_{\text{eq}}/\tilde{B}_{\text{eq}}$ between the expressions for $\partial\Pi/\partial\tilde{A}_{\text{eq}}$ and $\partial\Pi/\partial\tilde{B}_{\text{eq}}$ leads to the following equation of the macroscopic yield locus

$$\frac{1}{\bar{\sigma}^2}\left(\frac{\partial \Pi}{\partial \tilde{B}_{\text{eq}}}\right)^2 + 2(g+1)(g+f)\cosh\left(\frac{1}{\bar{\sigma} y_2}\frac{\partial \Pi}{\partial \tilde{A}_{\text{eq}}}\right) - (g+1)^2 - (g+f)^2 = 0 \tag{B.10}$$

Using $(\text{B.7})_1$ in $(\text{B.9})_1$ and the property that $\mathbf{Q} : \hat{\mathbb{p}} : \mathbf{R} = 0$, we see that

$$\frac{\partial \Pi}{\partial \tilde{A}_{\text{eq}}} = q_1 \frac{3y_2}{\bar{F}}(\boldsymbol{\Sigma} : \mathbf{X}), \qquad q_1 \equiv \sqrt{1 + \frac{R_{\text{eq}}^2}{\hat{h}_q}} \geq 1 \tag{B.11}$$

Similarly, using $(\text{B.7})_2$ in $(\text{B.9})_2$, we obtain

$$\left(\frac{\partial \Pi}{\partial \tilde{B}_{\text{eq}}}\right)^2 = \frac{q_2}{\bar{H}^2}\frac{3}{2}[\boldsymbol{\Sigma}' - \frac{2y_2\bar{G}}{\bar{F}}(\boldsymbol{\Sigma} : \mathbf{X})\hat{\mathbb{p}} : \mathbf{Q}] : \mathbb{p} : [\boldsymbol{\Sigma}' - \frac{2y_2\bar{G}}{\bar{F}}(\boldsymbol{\Sigma} : \mathbf{X})\hat{\mathbb{p}} : \mathbf{Q}] \tag{B.12}$$

where the dependency on tensor $\mathbf{R}$ is lumped into a parameter q_2

$$q_2 \equiv 1 + \frac{6y_2^2\bar{G}^2(\boldsymbol{\Sigma} : \mathbf{X})^2 R_{\text{eq}}^2 - 4y_2\bar{F}\bar{G}(\boldsymbol{\Sigma} : \mathbf{X})(\boldsymbol{\Sigma} : \mathbf{R})}{[\bar{F}\boldsymbol{\Sigma}' - 2y_2\bar{G}(\boldsymbol{\Sigma} : \mathbf{X})\hat{\mathbb{p}} : \mathbf{Q}] : \mathbb{p} : [\bar{F}\boldsymbol{\Sigma}' - 2y_2\bar{G}(\boldsymbol{\Sigma} : \mathbf{X})\hat{\mathbb{p}} : \mathbf{Q}]}, \qquad q_2 \leq 1 \tag{B.13}$$

The result that $q_2 \leq 1$ may be verified by evaluating $(\partial\Pi/\partial\tilde{B}_{\text{eq}})^2$ by combining forms $(\text{B.6})_2$ and $(\text{B.7})_2$ for $\partial\Pi/\partial\tilde{\mathbf{B}}$ in $(\text{B.9})_2$ and recalling that $\tilde{\mathbf{B}} = \bar{H}\boldsymbol{\beta}$. Also note that in the special cases of spherical void shapes or non-spherical voids subjected to axisymmetric deformation about the void axis $\underline{e}_3$, $\mathbf{R} \equiv \mathbf{0}$ and $q_1 = q_2 = 1$.

Using (B.11) and (B.12) in (B.10) leads to the desired result (40). In the latter, the criterion parameters are related to constants $\bar{F}$, $\bar{G}$ and $\bar{H}$ (Approximation $\mathcal{A}_2$) through

$$\kappa \equiv \frac{3}{\bar{F}}, \quad C \equiv \frac{1}{\bar{H}^2}, \quad \eta \equiv -\frac{2y_2\bar{G}}{\bar{F}}, \quad g \equiv \begin{cases} 0 & \text{(p)} \\ y_2 & \text{(o)} \end{cases} \tag{B.14}$$

while α_2 is defined by (B.2) above.

Appendix C. Criterion Parameters

C.1 Expressions

There are six parameters which depend on the microstructural variables f and w and on the anisotropy tensor $\mathbb{h}$: C, g, κ, η and α_2, listed by order of appearance in criterion (40)

or its final form (44), and α_1, which mainly appears in the evolution law of w. We first provide their expressions in closed form then present their derivation in the following sections.

$$g = 0 \quad \text{(p)}; \qquad g = \frac{e_2^3}{\sqrt{1-e_2^2}} = f\frac{e_1^3}{\sqrt{1-e_1^2}} = f\frac{(1-w^2)^{\frac{3}{2}}}{w} \quad \text{(o)} \tag{C.1}$$

We recall that e_1 and e_2 are the eccentricities of the void and the outer boundary of the RVE, respectively. Both are implicit functions of f and w.

$$\kappa = \begin{cases} \sqrt{3}\left\{\dfrac{1}{\ln f}\left[\dfrac{2}{3}\ln\dfrac{1-e_2^2}{1-e_1^2} + \dfrac{3+e_2^2}{3+e_2^4} - \dfrac{3+e_1^2}{3+e_1^4} + \dfrac{1}{\sqrt{3}}\left(\tan^{-1}\dfrac{e_2^2}{\sqrt{3}} - \tan^{-1}\dfrac{e_1^2}{\sqrt{3}}\right)\right.\right. \\ \qquad \left.\left. -\dfrac{1}{2}\ln\dfrac{3+e_2^4}{3+e_1^4}\right]\dfrac{4\hat{h}_q + 8\hat{h}_a - 7\hat{h}_t}{10} + \dfrac{4(\hat{h}_q + 2\hat{h}_a + 2\hat{h}_t)}{15}\right\}^{-1/2} & \text{(p)} \\ \dfrac{3}{2}\left(\dfrac{\hat{h}_q + 2\hat{h}_a + 2\hat{h}_t}{5}\right)^{-1/2}\left\{1 + \dfrac{(g_f - g_1) + \frac{4}{5}(g_f^{5/2} - g_1^{5/2}) - \frac{3}{5}(g_f^5 - g_1^5)}{\ln\frac{g_f}{g_1}}\right\}^{-1} & \text{(o)} \end{cases} \tag{C.2}$$

where $\hat{h}_q$, $\hat{h}_t$ and $\hat{h}_a$ are defined by (37) and (A.5), and

$$g_f \equiv \frac{g}{g+f}, \quad g_1 \equiv \frac{g}{g+1}$$

$$\alpha_2 = \begin{cases} \dfrac{(1+e_2^2)}{(1+e_2^2)^2 + 2(1-e_2^2)} & \text{(p)} \\ \dfrac{(1-e_2^2)(1-2e_2^2)}{(1-2e_2^2)^2 + 2(1-e_2^2)} & \text{(o)} \end{cases} \tag{C.3}$$

$$\eta = -\frac{2}{3\hat{h}_q}\frac{\kappa Q^*(g+1)(g+f)\mathrm{sh}}{(g+1)^2 + (g+f)^2 + (g+1)(g+f)[\kappa H^*\mathrm{sh} - 2\mathrm{ch}]},$$

$$C = -\frac{2}{3}\frac{\kappa(g+1)(g+f)\mathrm{sh}}{(Q^* + \frac{3}{2}\hat{h}_q\eta H^*)\eta}, \quad \mathrm{sh} \equiv \sinh(\kappa H^*), \quad \mathrm{ch} \equiv \cosh(\kappa H^*) \tag{C.4}$$

where $H^* \equiv 2\sqrt{\hat{h}_q}(\alpha_1 - \alpha_2)$ and $Q^* \equiv \sqrt{\hat{h}_q}(1-f)$.

$$\alpha_1 = \begin{cases} \left[e_1 - (1-e_1^2)\tanh^{-1}e_1\right]/(2e_1^3) & \text{(p)} \\ \left[-e_1(1-e_1^2) + \sqrt{1-e_1^2}\sin^{-1}e_1\right]/(2e_1^3) & \text{(o)} \end{cases} \tag{C.5}$$

Note that the expressions of α_2 and α_1 are identical to those given by (Gologanu et al., 1997) for isotropic matrices. $(\mathrm{C.1})_2$ derives directly from $(\mathrm{B.14})_4$ and $y_2 = c^3/a_2b_2^2$.

C.2 Derivation of κ and α_2

Most important among all criterion parameters are κ and α_2 which enter the "cosh" term in yield criterion (44). Both are affected by factors B_{2m} $(m = 0, 1, 2)$ of the velocity field. Note that α_2 enters the definition of the axisymmetric tensor $\mathbf{X}$ (42) which depends on the void axis $\underline{e}_3$. For consistency, it is required that the criterion be independent of

the void orientation in the limit of a spherical void, which implies that $\mathbf{X}$ must reduce to an isotropic tensor (i.e. $\alpha_2 = 1/3$). We satisfy this requirement by constraining the parameters B_{2i} to be independent of material anisotropy so that α_2 remains independent of $\mathbb{h}$; see equation (B.2). To obtain κ, we start from $(\text{B.14})_1$ where $\bar{F}$ is defined through

$$\bar{F} = \left(\ln \frac{u_1}{u_2}\right)^{-1} \inf_{[B_{20},B_{21},B_{22}]\in\mathbb{R}^3} \int_{u_2}^{u_1} F(u) \frac{du}{u} \tag{C.6}$$

by virtue of approximation $\mathcal{A}_2$. The true function that minimizes the above integral and the overall dissipation under purely hydrostatic loading was plotted in Figs. 15 and 16 as special cases of the family of functions designated $F^{\min}(u)$ in Appendix A. In seeking a closed form expression for $\bar{F}$ and κ, we must approximate $F^{\min}(u)$ by a function $F^{\text{app}}(u)$ since the former can only be evaluated numerically[6]. This is done in two steps, in the spirit of Gologanu et al. (1997). First, the specific values of B_{20}, B_{21} and B_{22} are obtained by minimizing the integrand $F(u)$ in (C.6) and not the integral itself (or equivalently $\Pi(\mathbf{D})$). The existence of the minimum is guaranteed by the convexity of $F(u)$ in the triplet B_{2m} (Keralavarma, 2008). This yields expressions for B_{2m} in terms of e, the eccentricity of the current confocal spheroid[7]. The function $F(u)$ that results from using the above values of B_{2m} has, however, a complicated expression and the integral (C.6) cannot be evaluated in closed form to calculate $\bar{F}$. Hence, in a second step, we recourse to heuristics. It is noted that this function has the form $\sqrt{\hat{h}_q F_q(e) + \hat{h}_t F_t(e) + \hat{h}_a F_a(e)}$ where the eccentricity e is used as the independent variable. Functions F_q, F_t and F_a are well approximated by functions of the form $C_1 \frac{(1-e^4)}{(3+e^4)^2} + C_2$, where C_1 and C_2 are determined by fitting the functions at the end points of the domain of e.

In the prolate case, the above procedure leads to the following approximate function $F^{\text{app}}(e)$

$$F^{\text{app}}(e) = \sqrt{\frac{9}{5}(4\hat{h}_q + 8\hat{h}_a - 7\hat{h}_t)\frac{(1-e^4)}{(3+e^4)^2} + 3\hat{h}_t} \qquad \text{(p)} \tag{C.7}$$

This approximation gives a close agreement with $F^{\min}(u)$, which minimizes the overall dissipation, regardless of the values of u_1 and u_2. In particular, $F^{\text{app}}(e)$ matches $F^{\min}(e)$ exactly in the limit cases of spherical ($e = 0$) or cylindrical ($e = 1$) void shapes. Fig. 15 compares the two functions for two different materials from Table 1 and a given microstructure ($f = 0.001$ and $w = 5$). In the case of oblate voids, however, the above procedure does not yield a satisfactory function $F^{\text{app}}(u)$ that minimizes the integral in (C.6). This is probably due to the stronger variations of $F^{\min}$ in that case, as illustrated in Fig. 16. We therefore propose the following heuristic function

$$F^{\text{app}}(u) = \sqrt{\frac{4}{5}(\hat{h}_q + 2\hat{h}_a + 2\hat{h}_t)}(1 + u + 2u^{5/2} - 3u^5) \qquad \text{(o)} \tag{C.8}$$

which captures the asymptotic behavior studied in Appendix A. The quality of this approximation is illustrated in Fig. 16. It provides a reasonable approximation of $F^{\min}(u)$.

[6]There is an abuse of language here since $F^{\min}$ is in fact $F^{\min}(u; \mathbb{h}, B_{2m}(u_1, u_2, \mathbb{h}))$ whereas the sought approximation $F^{\text{app}}(u; \mathbb{h})$ lives in a different functional space.

[7]The expressions of Gologanu et al. (1997) for B_{2m} also depended on e_2, due to the constraint (24). However, we choose to ignore this dependency, effectively constraining $\underline{v}^A$ to be homogeneous on every confocal spheroid, which is possible since B_{2m} are treated as functions of e rather than constants.

Finally, parameter κ is obtained in either case by substituting F^{app} given by (C.7) or (C.8) into (C.6) then using equation (B.14)$_1$. For the prolate case, since the integral can still not be evaluated in closed form, the mean of $F^{\text{app}2}(e)$ is evaluated using equation (C.6) and the square root of this value is assigned to $\bar{F}$. It is verified numerically that for all values of e_1 and e_2, the two values are close to each other. The final expressions are given by (C.2). The determination of α_2 is based on the factors B_{2m} determined after step 1 of the above procedure. Based on definition (B.2), this leads to the expressions (C.3), which are identical to those obtained by Gologanu et al. (1997) although the $B_{2m}(e)$ expressions used are not the same.

C.3 Parameters C and η

The parameters C and η are tied to the constants $\bar{G}$ and $\bar{H}$ by equations (B.14)$_{2,3}$. These are determined by forcing the approximate analytical yield locus to pass through and be tangent to known points on the exact two field yield locus (i.e. the yield locus defined by equations (5) and (28) without the approximations $\mathcal{A}_2$ and $\mathcal{A}_3$). Specifically, we seek to identify exact points on the yield locus for states of purely axisymmetric deformation for which $\boldsymbol{\beta} \propto \mathbf{Q}$. As can be inferred from (B.3)$_2$, this corresponds to stress states of the form $\boldsymbol{\Sigma} = \Sigma_{\text{m}}\mathbf{I} + \Sigma^{'}\hat{\mathbb{p}} : \mathbf{Q}$. In this case, the derivatives of the plastic dissipation, $\partial\Pi/\partial A$ and $\partial\Pi/\partial\beta_{ij}$ can be evaluated exactly for the points corresponding to $A = 0$, i.e., purely deviatoric loadings. Using equations (B.4), we obtain

$$\begin{aligned} \boldsymbol{\Sigma} : \mathbf{X} &= \pm 2\bar{\sigma}\sqrt{\hat{h}_q}(\alpha_1 - \alpha_2) \\ \boldsymbol{\Sigma}^{'} &= \pm\frac{2}{3}\frac{\bar{\sigma}}{\sqrt{\hat{h}_q}}(1-f)\hat{\mathbb{p}} : \mathbf{Q} \end{aligned} \tag{C.9}$$

In equation (C.9)$_1$, the parameter α_1 is defined in a manner similar to α_2 in (B.2), i.e., by

$$\alpha_1 \equiv \frac{D_{11}^{vA}}{2D_{11}^{vA} + D_{33}^{vA}} \tag{C.10}$$

where $\mathbf{D}^{vA}$ is the contribution to the average deformation rate of the void due to the velocity field $\underline{v}^A$, defined as in equation (52) with the components of $\underline{v}$ replaced by those of $\underline{v}^A$. The two algebraic equations that result from (i) substituting the above exact points in the equation of the analytical yield locus (44); and (ii) equating the slopes of the analytical and exact two-field yield loci at these points, can be solved for the values of the two unknown parameters $\bar{G}$ and $\bar{H}$, or equivalently C and η. This results in the expressions (C.4) given above.

Parameter α_1, which enters in both η and C through the term H^*, also enters the evolution law (55) of the void aspect ratio. Its expression is determined in a manner identical to that in (Gologanu et al., 1997). Similar to the case of α_2, which was found to be closely approximated by a function of e_2 alone, it is assumed that α_1 depends only on e_1 (or S) and is independent of f. Then α_1 can be evaluated by letting the boundary of the RVE tend to infinity (i.e. $a_2, b_2 \to \infty$ or $f \to 0$). Under these circumstances, one must take $B_{20} = B_{21} = 0$ for the velocity fields to be bounded. The remaining parameter B_{22} is then fixed by the boundary conditions and the components of $\mathbf{D}^{vA}$ can be evaluated in closed form, thus leading to the final expression (C.5) using (C.10). In the limit of a spherical void $\lim_{w\to 1} \alpha_1 = 1/3$

Appendix D. Rationale for Approximation $\mathcal{A}_3$

Since the first two terms in yield criterion (40) are non-negative quantities, it is clear that replacing q_1 and q_2 by lower bound estimates will lead to an upper bound to the yield criterion. However, as was shown in Appendix B, $q_2 \leq 1$ and hence, in general, approximation $\mathcal{A}_3$ does not preserve the upper bound character. In order to estimate the error entailed by $\mathcal{A}_3$, consider the case of small porosities, say $f < 0.1$. Tensor $\mathbf{R}$ is evaluated from its definition (B.8) using A and $\boldsymbol{\beta}$ from (B.3). A and $\boldsymbol{\beta}$ are determined by $\mathbf{D}$, which is evaluated from the yield function (40) using the normality rule and neglecting the derivatives of q_1 and q_2 with respect to $\boldsymbol{\Sigma}$. Expanding the resulting expression for $\mathbf{R}$ in a power series in the porosity f and keeping only the leading term, one may verify that $\mathcal{A}_3$ preserves the upper bound character for special loadings of the type $\boldsymbol{\Sigma}^{'} = \mathbf{0}$ (hydrostatic loading) and $\boldsymbol{\Sigma} : \mathbf{X} = 0$ (equivalent of deviatoric loading for non-spherical voids). Also, we remark that approximation $\mathcal{A}_3$ is exact in certain special cases such as spherical voids or non-spherical voids subjected to axisymmetric deformation about the void axis, as shown in Appendix B. For general loadings, one can show that the errors in the value of the yield function due to $\mathcal{A}_3$ are at least an order of magnitude smaller than f, which should be negligible for all practical purposes. Hence $\mathcal{A}_3$ is expected to be a good approximation at small porosities.

References

Benzerga, A. A., 2000. Rupture ductile des tôles anisotropes. Ph.D. thesis, Ecole Nationale Supérieure des Mines de Paris.

Benzerga, A. A., 2002. Micromechanics of Coalescence in Ductile Fracture. J. Mech. Phys. Solids 50, 1331–1362.

Benzerga, A. A., Besson, J., 2001. Plastic potentials for anisotropic porous solids. Eur. J. Mech. 20 (3), 397–434.

Benzerga, A. A., Besson, J., Batisse, R., Pineau, A., 2002. Synergistic effects of plastic anisotropy and void coalescence on fracture mode in plane strain. Modelling Simul. Mater. Sci. Eng. 10, 73–102.

Benzerga, A. A., Besson, J., Pineau, A., 1999. Coalescence–Controlled Anisotropic Ductile Fracture. J. Eng. Mat. Tech. 121, 221–229.

Benzerga, A. A., Besson, J., Pineau, A., 2004. Anisotropic ductile fracture. Part II: theory. Acta Mater. 52, 4639–4650.

Besson, J., Foerch, R., 1997. Large scale object oriented finite element code design. Comput. Methods Appl. Mech. Engrg 142, 165–187.

Budiansky, B., Hutchinson, J. W., Slutsky, S., 1982. Void growth and collapse in viscous solids. In: Hopkins, H. G., Sowell, M. J. (Eds.), Mechanics of Solids, The Rodney Hill 60th Anniversary Volume. Pergamon press, pp. 13–45.

Danas, K., Ponte Castañeda, P., 2009. A finite-strain model for anisotropic viscoplastic porous media: I–Theory. European Journal of Mechanics/A Solids 28, 387–401.

Eshelby, J., 1957. The determination of the elastic field of an ellipsoidal inclusion, and related problems. Proc. Roy. Soc A241, 357–396.

Garajeu, M., Michel, J. C., Suquet, P., 2000. A micromechanical approach of damage in viscoplastic materials by evolution in size, shape and distribution of voids. Comput. Methods Appl. Mech. Engrg 183, 223–246.

Gologanu, M., 1997. Etude de quelques problèmes de rupture ductile des métaux. Ph.D. thesis, Université Paris 6.

Gologanu, M., Leblond, J.-B., Devaux, J., 1993. Approximate models for ductile metals containing non-spherical voids – case of axisymmetric prolate ellipsoidal cavities. J. Mech. Phys. Solids 41 (11), 1723–1754.

Gologanu, M., Leblond, J.-B., Devaux, J., 1994. Approximate Models for Ductile Metals Containing Non–spherical Voids — Case of Axisymmetric Oblate Ellipsoidal Cavities. J. Eng. Mat. Tech. 116, 290–297.

Gologanu, M., Leblond, J.-B., Perrin, G., Devaux, J., 1997. Recent extensions of Gurson's model for porous ductile metals. In: Suquet, P. (Ed.), Continuum Micromechanics, CISM Lectures Series. Springer, New York, pp. 61–130.

Gologanu, M., Leblond, J.-B., Perrin, G., Devaux, J., 2001. Theoretical models for void coalescence in porous ductile solids – I: Coalescence in "layers". Int. J. Solids Structures 38, 5581–5594.

Gradshteyn, I., Ryzhik, I., 1980. Table of Integrals, Series, and Products. Academic Press, Inc.

Gurson, A. L., 1977. Continuum Theory of Ductile Rupture by Void Nucleation and Growth: Part I– Yield Criteria and Flow Rules for Porous Ductile Media. J. Eng. Mat. Tech. 99, 2–15.

Hill, R., 1948. A theory of yielding and plastic flow of anisotropic solids. Proc. Roy. Soc. London A 193, 281–297.

Hill, R., 1967. The essential structure of constitutive laws for metal composites and polycrystals. J. Mech. Phys. Solids 15, 79–95.

Kailasam, M., Ponte Castaneda, P., 1998. A general constitutive theory for linear and nonlinear particulate media with microstructure evolution. J. Mech. Phys. Solids 46 (3), 427–465.

Keralavarma, S. M., 2008. A Micromechanics based Ductile Damage Model for Anisotropic Titanium Alloys. Master's thesis, Texas A&M University, USA.

Keralavarma, S. M., Benzerga, A. A., 2008. An approximate yield criterion for anisotropic porous media. C. R. Mecanique 336, 685–692.

Koplik, J., Needleman, A., 1988. Void growth and coalescence in porous plastic solids. Int. J. Solids Structures 24 (8), 835–853.

Leblond, J., Gologanu, M., 2008. External estimate of the yield surface of an arbitrary ellipsoid containing a confocal void. C. R. Mecanique 336, 813–819.

Leblond, J. B., 2003. Mécanique de la rupture fragile et ductile. Hermes Science Publications, Lavoisier.

Leblond, J.-B., Mottet, G., 2008. A theoretical approach of strain localization within thin planar bands in porous ductile materials. C. R. Mecanique 336, 176–189.

Lee, B. J., Mear, M. E., 1992. Axisymmetric deformation of power–law solids containing a dilute concentration of aligned spheroidal voids. J. Mech. Phys. Solids 40 (8), 1805–1836.

Mandel, J., 1964. Contribution théorique à l'étude de l'écrouissage et des lois d'écoulement plastique. In: 11^{th} International Congress on Applied Mechanics. Springer, Berlin, pp. 502–509.

McClintock, F. A., 1968. A criterion for ductile fracture by the growth of holes. J. App. Mech. 35, 363–371.

Monchiet, V., Cazacu, O., Charkaluk, E., Kondo, D., 2008. Macroscopic yield criteria for plastic anisotropic materials containing spheroidal voids. Int. J. Plasticity 24, 1158–1189.

Pardoen, T., Hutchinson, J. W., 2000. An extended model for void growth and coalescence. J. Mech. Phys. Solids 48, 2467–2512.

Perrin, G., 1992. Contribution à l'étude théorique et numérique de la rupture ductile des métaux. Ph.D. thesis, Ecole Polytechnique.

Pineau, A., 2006. Development of the local approach to fracture over the past 25 years: theory and applications. Int. J. Frac. 138, 139–166.

Pineau, A., Pardoen, T., 2007. Failure of Metals. Comprehensive Structural Integrity 2, 684–797, Chapter 2.06.

Ponte Castañeda, P., Zaidman, M., 1994. Constitutive models for porous materials with evolving microstructure. J. Mech. Phys. Solids 42, 1459–1495.

Ponte Castaneda, P., 1991. The effective mechanical properties of nonlinear composites. J. Mech. Phys. Solids 39, 45–71.

Rice, J. R., Tracey, D. M., 1969. On the enlargement of voids in triaxial stress fields. J. Mech. Phys. Solids 17, 201–217.

Riks, E., 1979. An incremental approach to the solution of snapping and buckling problems. Int. J. Solids Structures 15, 529–551.

Scheyvaerts, F., Pardoen, T., Onck, P. R., 2010. A new model for void coalescence by internal necking. International Journal of Damage Mechanics 19, 95–126.

Sovik, O., Thaulow, C., 1997. Growth of spheroidal voids in elastic–plastic solids. Fatigue Fract. Engng. Mater. Struct. 20, 1731–1744.

Suquet, P., 1982. Plasticité et homogénéisation. Thèse d'Etat, Université Pierre et Marie Curie – Paris VI.

Tvergaard, V., 1982. On localization in ductile materials containing spherical voids. Int. J. Frac. 18, 237–252.

Tvergaard, V., 1990. Material failure by void growth to coalescence. Advances in Applied Mechanics 27, 83–151.

Tvergaard, V., Needleman, A., 1984. Analysis of the cup–cone fracture in a round tensile bar. Acta metall. 32, 157–169.